# Exploring the Correlation Between Functional Gradients in Material Properties and Solute Diffusion Across the Osteochondral Interface





# Exploring the Correlation Between Functional Gradients in Material Properties and Solute Diffusion Across the Osteochondral Interface

Ву

## Jordi Dominique Cazier

in partial fulfilment of the requirements for the degree of

#### **Master of Science**

in Biomedical Engineering

at the Delft University of Technology, to be defended publicly on Thursday September 21, 2023 at 10:00 AM.

Student number: 4980255

Supervisors: Prof.dr. G.J.V.M. van Osch Erasmus MC & TU Delft

Dr. M.J. Mirzaali
Dr. V. Arbabi
TU Delft
UMC Utrecht

Thesis committee: Prof.dr. G.J.V.M. van Osch Erasmus MC & TU Delft

Dr.ir. A.C. Akyildiz TU Delft ir. L.B. Kunkels TU Delft Dr. M.J. Mirzaali TU Delft

An electronic version of this thesis is available at <a href="http://repository.tudelft.nl/">http://repository.tudelft.nl/</a>.



# For my mother who will always be in my heart

# **Contents**

| Abstract  | 8  |
|---|----|
| 1 Introduction  | 10 |
| 1.1 Structure and Organization of the Osteochondral Interface | 12 |
| 1.2 Research Questions  | 15 |
| 2 Materials and Methods                                       |    |
| 2.1.1 Geometry  | 18 |
| 2.1.2 Mechanical and Physical Properties                      | 19 |
| 2.1.3 Initial and Boundary Conditions                         | 21 |
| 2.1.4 Validation  | 22 |
| 2.1.5 Near-Equilibrium Concentration Time                     | 22 |
| 2.2 Diffusion Experiments                                     | 22 |
| 2.2.1 Sample Preparation                                      | 22 |
| 2.2.2 Image Acquisition                                       | 25 |
| 2.2.3 Image Processing  | 25 |
| 3 Results   |    |
| 00.3.1.1 Validation of Refinement                             | 27 |
| 3.1.2 Near-Equilibrium Concentration Time                     | 27 |
| 3.2 Diffusion Experiments                                     | 30 |
| 4 Discussion  |    |
| 4.2 Experiments   | 35 |
| 4.2.1 3D-Printing   | 35 |
| 4.2.2 Diffusion Experiments                                   | 35 |
| 4.3 Recommendations   | 36 |
| 5 Conclusion  | 40 |
| Appendix B  |    |

# **Abstract**

The solute transport across the osteochondral (OC) interface is of crucial metabolic importance for a normal function of articular cartilage, and, therefore, for the OC interface as a whole. A better understanding how the mechanical- and physiological properties of the OC interface affect the solute transport across the OC interface could lead to new insights in repair strategies. The aim of this master's thesis was to investigate how graded mechanical- and/or physiological properties of the OC interface affect the solute transport across the OC interface.

A combination of computational modelling and experimental diffusion tests on GelMA-based hydrogel plugs was used to approach the goal. Regarding the computational model, first, a multi-zone biphasic-solute finite element model that accurately replicates axial solute transport across the OC interface was designed and validated. Second, a power law function was used to apply several gradients on the initial values of the solid volume fraction (SVF), diffusion coefficient, and elastic modulus across the OC interface to study the effect of each parameter on the solute diffusion across the OC interface. On the experimental front, attempts were made to 3D-print GelMA-based hydrogel plugs but all failed. Alternatively, five groups (n = 3) of hydrogel plugs were created, each of which underwent different UV curing time, by casting GelMA into cylindrical plugs. Axial diffusion of an alizarin red solution through the hydrogel samples was recorded using a digital camera.

The results of the computational model show that only the SVF plays a small role in the height of the equilibrium concentration reached in the subchondral bone layer. However, the influence of both the SVF and diffusion coefficient on the time when the equilibrium concentration is reached in the subchondral bone is considerably large. It is shown that the elastic modulus has a negligible influence on the solute transport. Regarding the experimental diffusion tests, air bubbles and/or sincere light reflections made all but six hydrogel plugs unusable for further analysis. A relationship between sample thickness and diffusion is observed in the remaining hydrogel samples. The results of the SVF computational model and experimental diffusion tests were compared, but sufficient experimental data was lacking to draw any solid conclusions from this comparison.

This master's thesis provides a new computational model of the OC interface which allows the implementation of graded parameters across the OC interface. It is concluded that the current experimental set-up is not suitable for obtaining consistent data on solute transport across hydrogel plugs. Suggestions to improve the experimental set-up are made.

# 1 Introduction

Osteoarthritis (OA) is the most common chronic musculoskeletal disease among elderly people, causing a structural degeneration of the articular cartilage (Oliviero et al., 2010). Such damage can progress to the underlying subchondral bone, which increases the risk to suffer pain and reduced mobility (Buckwalter & Mankin, 1998). One of the parameters that changes because of OA is the molecular diffusion between articular cartilage and the bone directly underneath the cartilage (Botter et al., 2011; Westacott, 2002). Because articular cartilage has a limited self-healing capacity, due to the lack of nerves (Dye et al., 1998) and a limited vascularity (Moses et al., 1990), the molecular diffusion of solutes through cartilage is of crucial metabolic importance for a normal function of cartilage (Leddy & Guilak, 2003). Despite extensive research, OA still has limited treatment possibilities (Tuan et al., 2013), predominantly due to the different healing capacities and mechanical properties of the bone and cartilage tissues (Di Martino et al., 2015), making the bonecartilage interface (also known as osteochondral (OC) interface) a complex, graded structure (Di Martino et al., 2015), where the structure, mechanical properties, and composition vary smoothly from the articular cartilage surface to the bone (Antons et al., 2018; Di Luca et al., 2015; Khorshidi & Karkhaneh, 2018).

In recent years, the regeneration of the whole OC interface has received an increased attention (Ansari et al., 2019; Di Martino et al., 2015). This increased popularity to repair the whole OC interface instead of just the articular cartilage or the bone finds its origin in some studies suggesting that OA is a disease that could affect the whole joint instead of just cartilage (Lories & Luyten, 2011; Mahjoub et al., 2012). Additionally, articular cartilage and bone are mechanically connected (Brown et al., 1984), so in case of a traumatic event or a disease like OA leading to an OC defect, not only the articular cartilage or bone, but both are affected (Pape et al., 2010). Consequently, in order to regenerate a functional OC interface, it is important that both cartilage and the underlying bone are reconstructed simultaneously (Ansari et al., 2019; Di Luca et al., 2015; Mukherjee et al., 2020; Peters et al., 2018), and that the biomechanical properties mimic those of the native OC interface (Liu et al., 2015). Among the materials used in tissue engineering, hydrogels have proven to be one of the most prestigious and multipurpose materials (Hunt et al., 2014; Wang et al., 2018). Hydrogels are 3D-networks composed of crosslinked hydrophilic polymer chains and water that fills the spaces between the polymer chains (Korah et al., 2018). The highly hydrated structure of hydrogels has great similarities with the natural extracellular matrix (Spicer, 2020).

Using conventional methods such as freeze-drying (Levingstone et al., 2014), solvent-casting (Eltom et al., 2019), and gas-forming (Loh & Choong, 2013), many types of scaffolds have been designed. However, up to date, no scaffold of the OC interface has been designed that reached the same level of efficiency as the native OC interface. With the introduction of (multi-material) 3D-printing, the qualities of the scaffolds, such as biocompatibility, mechanical stiffness (Chen et al., 2012), and low brittleness (Rastogi & Kandasubramanian, 2019), have significantly improved compared to the conventional scaffolds (Varma et al., 2020; Zhang et al., 2020). Moreover, 3D-printing techniques allow the production of interconnected porous scaffolds with highly controlled pore geometry such that the morphologic properties match those of the host tissue (Zhang et al., 2020). Because 3D-printing allows to create graded scaffolds with various types of biomaterials, structures, and mechanical properties (Chen et al., 2019; Doubrovski et al., 2015; Nowicki et al., 2020), it makes it possible to study how important the contribution of each mechanistic and material mechanism is, and how one mechanism affects of the others.

As mentioned earlier, one of the parameters that is affected due to OA is the molecular diffusion through the OC interface (Botter et al., 2011; Westacott, 2002), which is of crucial metabolic importance for a normal function of the cartilage (Leddy & Guilak, 2003) and, therefore, for the whole OC interface. The diffusion through the OC interface does not only depend on the morphological characteristics like porosity and thickness of the OC interface, which could be replicated with 3D-printing techniques (Zhang et al., 2020), but also on the distribution and concentration of the extracellular matrix components (proteoglycans and collagen fibrils) which contribute to the mechanical properties of the OC interface (Arbabi et al., 2016; Botter et al., 2011). Hence, in 3D-printing, it is important that the biological and mechanical properties of the ink used match those of the native tissue. As mentioned before, the structures of hydrogels have great similarities with the natural extracellular matrix (Spicer, 2020). Among various types of hydrogel inks, the inks based on gelatine functionalized with methacryloyl groups (GelMA) show great promise due to their excellent biocompatibility, on-demand photocrosslinkability, and highly tuneable physicochemical properties of this collagen-modified biopolymer (Daly et al., 2016) which makes it possible to apply structural and mechanical gradients. A deeper understanding of how gradients in different mechanical and/or physiological properties affect the diffusive behaviour within the OC interface could improve the development of current regenerative methods.

Hence, the main goal of this master's thesis is to investigate how graded mechanical- and/or physiological properties of the OC interface affect the solute transport across the OC interface.

However, *in vivo* and *in vitro* experiments are often associated with high costs and time-consuming analysis. Meanwhile, the budget and time span for this master's thesis are not unlimited. A solution to overcome these drawbacks is the use of computational models. Computational models concurrently calculate the mechanical and physiological behaviour of multiple tissues, and so, once properly validated, could provide valuable insights in tissue interactions that are difficult to obtain through traditional experimental methods. Moreover, the parameter values within a computational model can easily be altered. Thus, a computational model could generate iterations of the same model with different parameter values and predict the effect of these different values on the modelled tissue(-s).

The main goal of this master's thesis is to investigate how graded mechanical- and/or physiological properties of the OC interface affect the solute transport across the OC interface. In this chapter, a detailed description of the structure and organization of the OC interface will be described, followed by the resulting research questions of this master's thesis.

## 1.1 Structure and Organization of the Osteochondral Interface

The mature OC interface of synovial joints consists of three tissue layers, varying in structure and mechanical properties: the compliant hyaline articular cartilage (HAC), a thin layer of articular calcified cartilage (ACC) and the rigid subchondral bone (SCB) (Figure 1.1). The function of the HAC is to act as a shock damper to transmit the loading forces in the articular joint with a minimal stress concentration (Bernstein et al., 2013; Broom & Thambyah, 2018), and to provide a smooth surface at the end of the bones which realizes near-frictionless movement in the joint (Broom & Thambyah, 2018). It is assumed that the main function of the ACC is to transmit the articular forces between the compliant HAC and the stiff SCB (Redler et al., 1975). Finally, the SCB contributes to the preservation of the functional integrity of the HAC (Duncan et al., 1987). Moreover, the SCB provides mechanical support for the HAC which is essential for the performance of the HAC (Nooeaid et al., 2012).

Healthy human HAC is composed of chondrocytes and a stiff viscoelastic extracellular matrix (ECM) (Cohen et al., 1998; Hoemann, 2004). Chondrocytes are responsible for the synthesis and maintenance of HAC, where the ECM provides the structure of the HAC and thus its unique mechanical properties. The ECM is comprised of proteoglycans, glycosaminoglycans (GAGs), water, collagen fibrils (mostly collagen type II (Buckwalter & Mankin, 1997)), and non-collagenous proteins (Hoemann, 2004). Collagen fibrils on their own do not provide significant resistance against

compression, they do however provide great resistance against tension and are responsible for the major part of the tensile properties of the HAC (Schmidt et al., 1990; Woo et al., 1976). The most abundant GAG-bearing proteoglycan in HAC is aggrecan (Hoemann, 2004). Attached to the proteoglycans are negatively charged GAGs that attract water into the ECM of HAC, thereby creating hydrated spaces in the ECM which functions as a porous-permeable reinforcement for the collagen and so provides the HAC its resistance against compression and thus its compressive strength (Setton et al., 1994).

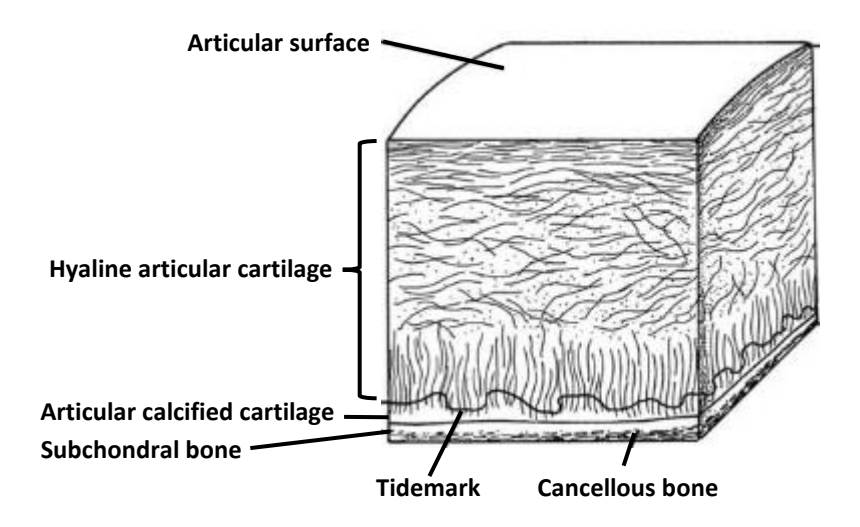


*Figure 1.1:* Schematic representation of the osteochondral tissue and the orientation and arrangement of the extracellular matrix fibers, modified from Di Luca et al. (2015).

The HAC is subdivided in three layers from the articular surface towards the bone: the superficial zone (SZ), middle zone (MZ), and the deep zone (DZ) (Figure 1.2), with a depth of 10-20%, 40-60%, and 30-40% of the total HAC height, respectively (Bullough & Goodfellow, 1968; Clark, 1985). Each layer differs in orientation, size, type, and structure of the collagen fibrils and chondrocytes (Figure 1.2). The SZ consists of dense collagen fibrils, and flat and ellipsoid chondrocytes which are oriented parallel to the articular surface, thereby creating a dense articular surface. Due to their parallel orientation, the collagen fibrils provide large resistance against tensile and shear forces (Bhosale & Richardson, 2008). In the MZ, the collagen fibrils are obliquely aligned to the articular surface (Figure 1.2). Furthermore, the chondrocytes are more spheroid-shaped, and the concentration is less than in the SZ (Figure 1.2). The GAG-bearing proteoglycans in the MZ reinforce the collagen fibrils in this zone, giving the HAC its compressive strength (Mansour, 2003). In the DZ, the collagen fibrils are stacked in columns perpendicular to the articular surface, while the chondrocytes are spheroid-shaped (Figure 1.2).

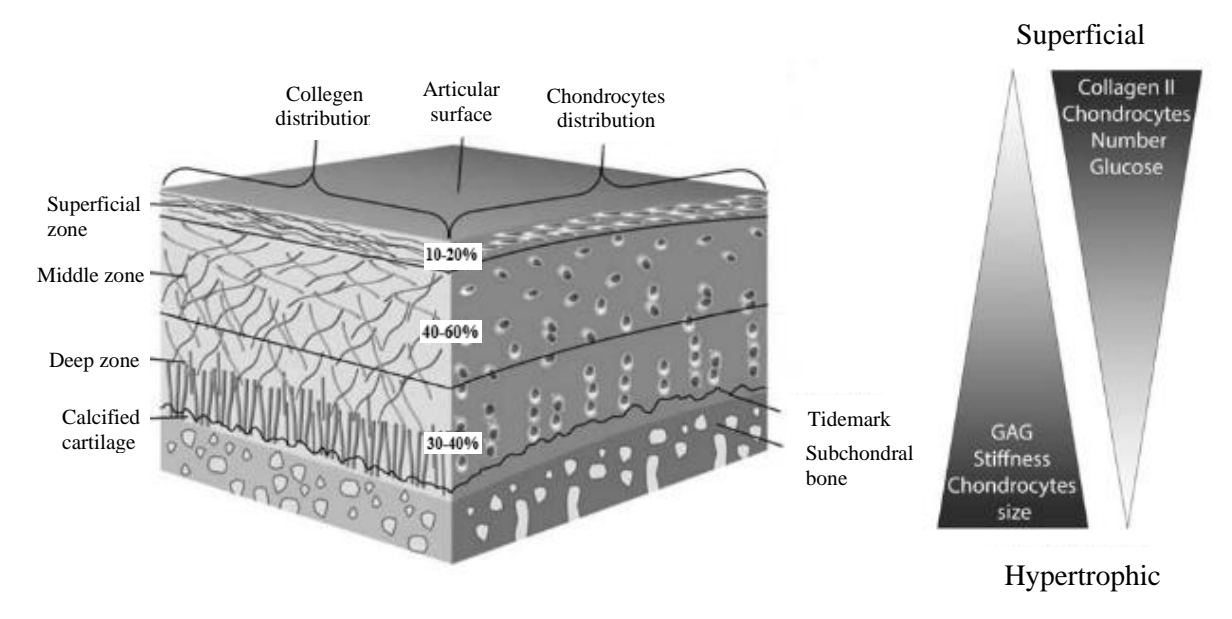


*Figure 1.2:* Schematic representation of the osteochondral interface, showing the orientation and arrangement of the collagen fibrils throughout the hyaline articular cartilage, modified from Di Luca et al. (2015).

Between the HAC and ACC, a distinct, wavy, jigsaw puzzle-like, line can be seen (Figure 1.2). As first described by Fawns & Landells (1953), this boundary between the HAC and ACC is called the tidemark. The biomechanical role of the jigsaw waviness of the tidemark is that it provides great resistance to shear stresses between HAC and SCB (Redler et al., 1975). Furthermore, the DZ of HAC is strongly connected with the ACC by collagen fibrils which cross from the DZ of the HAC through the tidemark into the ACC layer (Redler et al., 1975). Within the ACC layer, the chondrocytes are more hypertrophic than in the HAC (Buckwalter et al., 1986). Due to these hypertrophic chondrocytes, collagen type X is synthesized (Kielty et al., 1985), and collagen type II fibrils degrade, leading to the formation of C-propeptide which binds calcium (Poole et al., 1989), mineralizing the ECM of ACC, providing a stiffer ECM than that of HAC, and thus influencing its material properties. Within the ACC layer, the mineral content and material properties are graded near the HAC at the tidemark (Gupta et al., 2005). Mente & Lewis (1994) stated that ACC is 10-100 times less stiff than SCB. Even when the ACC and SCB have the same mineral content, ACC is less stiff than SCB due to the organization and distribution of the mineralized tissue and collagen fibrils (Gupta et al., 2005). Summarized, the integrity and the shock-absorbing function of the ACC layer is provided by the graded mineralized ECM of ACC in the presence of collagen type X.

Underneath the ACC lies the dense SCB. The wavy boundary between the ACC and SCB is called the cement line. As mentioned earlier, the main function of the SCB is to provide mechanical support

for the HAC which is essential for the performance of the HAC (Nooeaid et al., 2012). Mainly collagen type I fibrils are found in the ECM of the SCB, mineralized by deposits of calcium and phosphate named hydroxyapatite (Heinegård & Oldberg, 1989). The hydroxyapatite and calcium are bound to the ECM of the SCB by the proteins osteocalcin and osteonectin, respectively (Heinegård & Oldberg, 1989). The dense SCB comprises of multiple bone plates of 0.2-0.4mm thickness joined together to embed intercommunicating spaces of 0.4-0.6mm thickness (Madry et al., 2010). Unlike the non-vascularized HAC, the SCB has a large quantity of arterial and venous vessels (Imhof et al., 1999). Occasional small branches of the vessels cross the cement line from the SCB into the ACC (Clark, 1990; Gilmore St. & Palfrey, 1987). However, no collagen fibrils are continuous between the SCB and ACC (Burr et al., 1988), making the cement line a region where the mechanical interlocking of the SCB and ACC is weak.

### 1.2 Research Questions

Summarized, the OC interface is a heterogeneous, anisotropic, multi-phasic, and nonlinear material. The diffusion of molecules through the OC interface is of crucial metabolic importance for a normal function of the cartilage (Leddy & Guilak, 2003), and, therefore, for the whole OC interface. Previously, research has been done on the regeneration of the whole OC interface. However, up to date, no scaffold of the OC interface has been designed that reached the same level of efficiency as the native OC interface. Knowledge how different mechanical- and physiological properties, such as the solid volume fraction, diffusion coefficient, and the elastic modulus, affect the diffusive behaviour within the OC interface could lead to new insights of how to replicate the diffusive behaviour of the OC interface and therefore improve the development of current regenerative methods. Therefore, the goal of this master's thesis is to investigate how graded mechanical- and/or physiological properties of the OC interface affect the solute transport across the OC interface. The main goal can be dissected into sub-questions. To what extent does the solid volume fraction, the diffusion coefficient, and the elastic modulus influence the solute transport across the OC interface?

To achieve this, a combination of a computational model and an experimental set-up is used. Regarding the computational model, first, a model that accurately replicates the diffusive behaviour of the OC interface is designed and validated. Second, a power law function is used to apply various gradients on the solid volume fraction, diffusion coefficient, and elastic modulus values of the computational model to study the effect of each parameter on the solute diffusion through the OC interface individually. On the experimental front, attempts are made to 3D-print a graded GelMA-based hydrogel that mimics the diffusive behaviour of the OC interface. The properties of the

hydrogel are graded by alternating the UV crosslinking time during the printing process. The relationship between UV curing time and solute transport across GelMA is investigated by performing diffusion tests.

# 2 Materials and Methods

# 2.1 Computational Model

Computational models based on biphasic-solute mixture models have proven to be able to describe the diffusion of neutral solutes through biphasic tissues like bone and cartilage (Arbabi et al., 2015, 2016; Ateshian et al., 2012; Mauck et al., 2003). The mixture in these models consists of a porous-permeable solid matrix, a solvent, and a solute (Ateshian et al., 2011; Mauck et al., 2003). The main objective of these mixture models is to solve for the three unknowns, being the motion of the solid matrix  $\boldsymbol{u}$ , the pressure of the fluid  $\boldsymbol{p}$ , and the solute concentration  $\boldsymbol{c}$ , using three governing equations (Ateshian et al., 2011; Mauck et al., 2003). These equations enforce the balance of the linear momentum for the mixture (eq. 1), the balance of the mass for the mixture (eq. 2), and the balance of the mass for the solute (eq. 3) (Ateshian et al., 2011; Mauck et al., 2003). The balance of linear momentum for the mixture could be described as:

$$div T = 0,$$
(1)

where **T** is the Cauchy stress tensor for the mixture which describes the total (mixture) stress. The balance of the mass of the mixture could be described as:

$$\operatorname{div}(\mathbf{v}^{S} + \mathbf{w}) = 0,$$

where  $\mathbf{v}^S$  is the velocity of the porous-permeable solid matrix, and  $\mathbf{w}$  describes the volumetric flux of the solvent relative to the solid with  $\varphi^w$  describing the volume fraction of the solvent in the mixture, and  $\mathbf{v}^w$  being the velocity of the solvent. At last, since the total amount of the solute in the bath and the tissue must remain constant, the equation of the balance of mass for the solute could be written as:

$$\frac{1}{J}\frac{D^s}{Dt}J\varphi^w\tilde{\kappa}\tilde{c}+div\,\mathbf{j}=0,$$

where  $J=\det \mathbf{F}$ , and  $\mathbf{F}$  is the deformation gradient of the solid matrix, and  $\frac{D^s}{Dt}$  is the material time derivative in the spatial frame, following the solid,  $\tilde{\kappa}$  is the effective solubility, c is the solute

concentration,  $\tilde{c}$  is the effective solute concentration ( $\tilde{c} = \frac{c}{\kappa}$ ) which is continuous across boundaries and contact surfaces (Ateshian et al., 2011), and  $\mathbf{j}$  is the molecular flux of the solute relative to the solid. The dependence of  $\mathbf{w}$  and  $\mathbf{j}$  on the solid matrix strain and effective solute concentration are shown by the following equations:

$$\mathbf{w} = -\widetilde{\mathbf{k}} \left( \operatorname{grad} \widetilde{p} + R\theta \frac{\widetilde{\kappa}}{d_0} \mathbf{d} \operatorname{grad} \widetilde{c} \right)$$
(4)

$$\mathbf{j} = \tilde{\kappa} \mathbf{d} \left( -\phi^{w} \operatorname{grad} \tilde{c} + \frac{\tilde{c}}{d_{0}} \mathbf{w} \right), \tag{5}$$

with

$$\widetilde{\mathbf{k}} = \left[ \mathbf{k}^{-1} + \frac{R\theta}{\varphi^w} \frac{\widetilde{\kappa} \widetilde{c}}{d_0} \left( \mathbf{I} - \frac{\mathbf{d}}{d_0} \right) \right]^{-1}$$

$$\varphi^w = 1 - \frac{\varphi_r^s}{J},$$
(6)

where  $\widetilde{\mathbf{k}}$  is the hydraulic permeability tensor for the flow of the solution,  $\widetilde{p}$  is the effective solute pressure which is the mechanical contribution of the total solute pressure  $(p=\widetilde{p}+R\theta\Phi)$ , R is the universal gas constant,  $\theta$  is the absolute temperature,  $\Phi$  is the osmotic coefficient,  $d_0$  is the diffusion coefficient tensor in free solution,  $\mathbf{d}$  is the solute diffusivity coefficient tensor in the mixture,  $\mathbf{k}$  is the hydraulic permeability tensor of the solvent through the solid matrix, and  $\varphi_r^s$  is the volume fraction of the solid phase in the reference configuration (Ateshian et al., 2011; Mauck et al., 2003).

By applying the principle of virtual work, the equations mentioned above were solved in the open-source finite element modelling program FEBio (v3.6.0) to describe the transport of a neutral solute through a biphasic structure.

## 2.1.1 Geometry

The mesh of a validated multi-layer, biphasic-solute model of the OC interface (Arbabi et al., 2016) was replicated and modified by a comprehensive mesh refinement for each layer of the OC interface (Figure 2.1). These mesh refinements allowed for the incorporation of depth-dependent variations for various tissue parameters through the individual layers of the OC interface and therefore the

(7)

possibility to apply gradients on the parameter values through the OC interface. A description of the geometry of the computational model is provided in the next section.

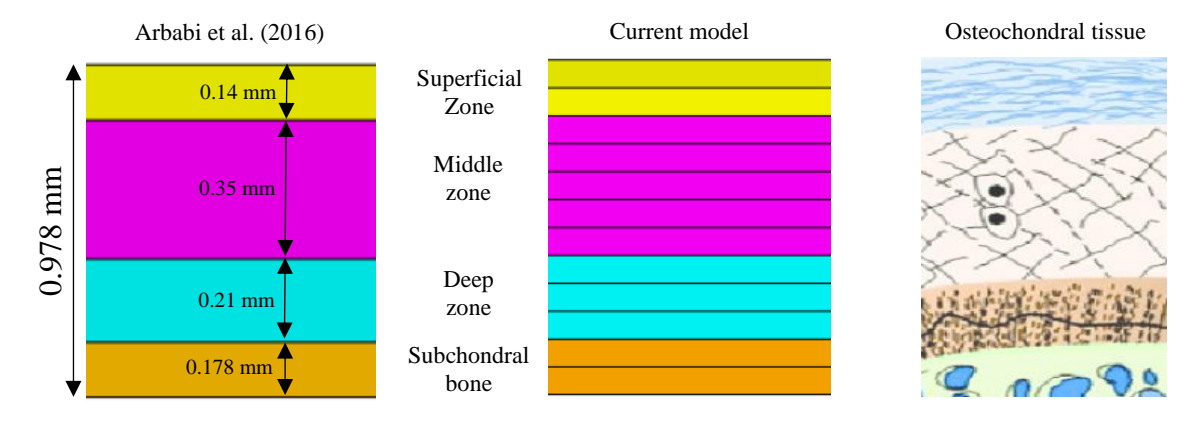


*Figure 2.1:* 2D schematic of the multi-zone model of the osteochondral interface of Arbabi et al. (2016) (left), the zonal refinement of the computational model as used in this study (middle), and the structure and organization of the osteochondral tissues (right).

The model comprised four different zones: SZ (20% HAC thickness), MZ (50% HAC thickness), DZ (30% HAC thickness), and SCB. The thickness of HAC (0.7 mm) and SCB (0.178 mm) was obtained from micro-CT images (Pouran et al., 2016). It was assumed that the diffusion of the solutes only occurred in the axial direction (Kulmala et al., 2010). On top of the cartilage was an overlaying bath of 12 mm high (Figure 2.2A), which corresponded to the diffusion experiments of Pouran et al. (2016). Each zone was then subdivided into multiple zones of equal height, such that the SZ/MZ/DZ/SCB comprised of 2/5/3/2 zones, respectively (Figure 2.1). Eight-node trilinear hexahedral elements were used for mesh generation, which were refined near the interfaces to ensure computational accuracy (Figure 2.2).

#### 2.1.2 Mechanical and Physical Properties

Both the HAC and the SCB were modelled as neo-Hookean material with a Poisson's ratio of 0, while the E modulus was selected in such a way that the swelling behaviour of the HAC resembles that of the experiments of Arbabi et al. (2015), meaning that the E modulus was chosen high enough to resist the osmotic pressure from the bath and large deformations were prevented. Both the hydraulic permeability tensor and the diffusion coefficient tensor for the bath, HAC and SCB were regarded as isotropic. The hydraulic permeability and the effective solubility were set to  $10^{-3}$  mm<sup>4</sup>/Ns and 1, respectively (Ateshian et al., 2012; Ateshian & Weiss, 2013). The solid volume fraction (SVF) of the SZ, MZ, and DZ were 0.2, 0.3, and 0.4, respectively (Sophia Fox et al., 2009), and the SVF of the SCB was set to 0.8 (Li & Aspden, 1997). The diffusion coefficient in the bath was set to 250  $\mu$ m<sup>2</sup>/s (Nair et al., 2008) and for the SZ, MZ, DZ, and SCB to 4.35, 0.40, 0.18, and 0.12  $\mu$ m<sup>2</sup>/s, respectively (Arbabi et al., 2016).

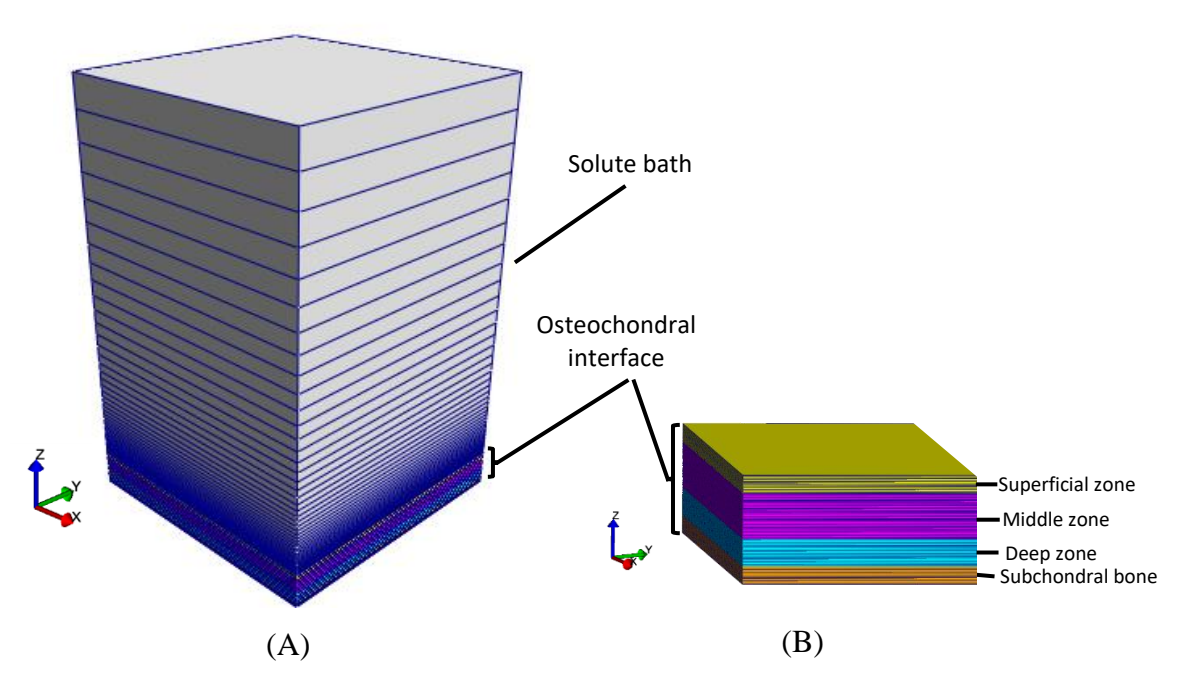


*Figure 2.2:* (A) Schematic drawing of the computational model including the solute bath and the osteochondral (OC) interface. (B) A closer look at the model including the four zones of the OC interface.

To obtain a gradient for the values of the diffusion coefficient, SVF, and E modulus through the OC interface, the following power law for material gradation is used (equation 8) (Chakraborty et al., 2003):

$$d_{y} = (d_{t} - d_{b}) \left(\frac{y}{z} + \frac{1}{2}\right)^{k} + d_{b},$$
(8)

where z is the total height of the OC interface, k is the power coefficient, and  $d_b$ ,  $d_t$ , and  $d_y$  are the diffusion coefficient at the bottom, top, and distance y from the middle of the OC interface, respectively. The range  $[d_t - d_b]$  of each parameter was set according to the values of the SZ and SCB layer used in the model of Arbabi et al. (2016). Hence, the range of the diffusion coefficient was  $[4.35 - 0.12] \, \mu \text{m}^2/\text{s}$ , the range of the SVF was set to [0.2 - 0.8]. The range of the E modulus was  $[10 - 1150] \, \text{MPa}$ , where the  $d_t$  value was taken from Arbabi et al. (2016) and the  $d_b$  value represents the average E modulus of human SCB (1.15 GPa) (Choi et al., 1990). The values of k = 0.015, 0.1, 1/3, 1, 2, and 3, were used to study the effect of different gradients of the selected parameters on the solute diffusion through the OC interface. Figure 2.3 shows the values of the SVF, diffusion coefficient, and E modulus through the OC interface obtained from Arbabi et al. (2016) and for each used gradient k in equation 8. An overview of the values used for each parameter is presented in Appendix A.

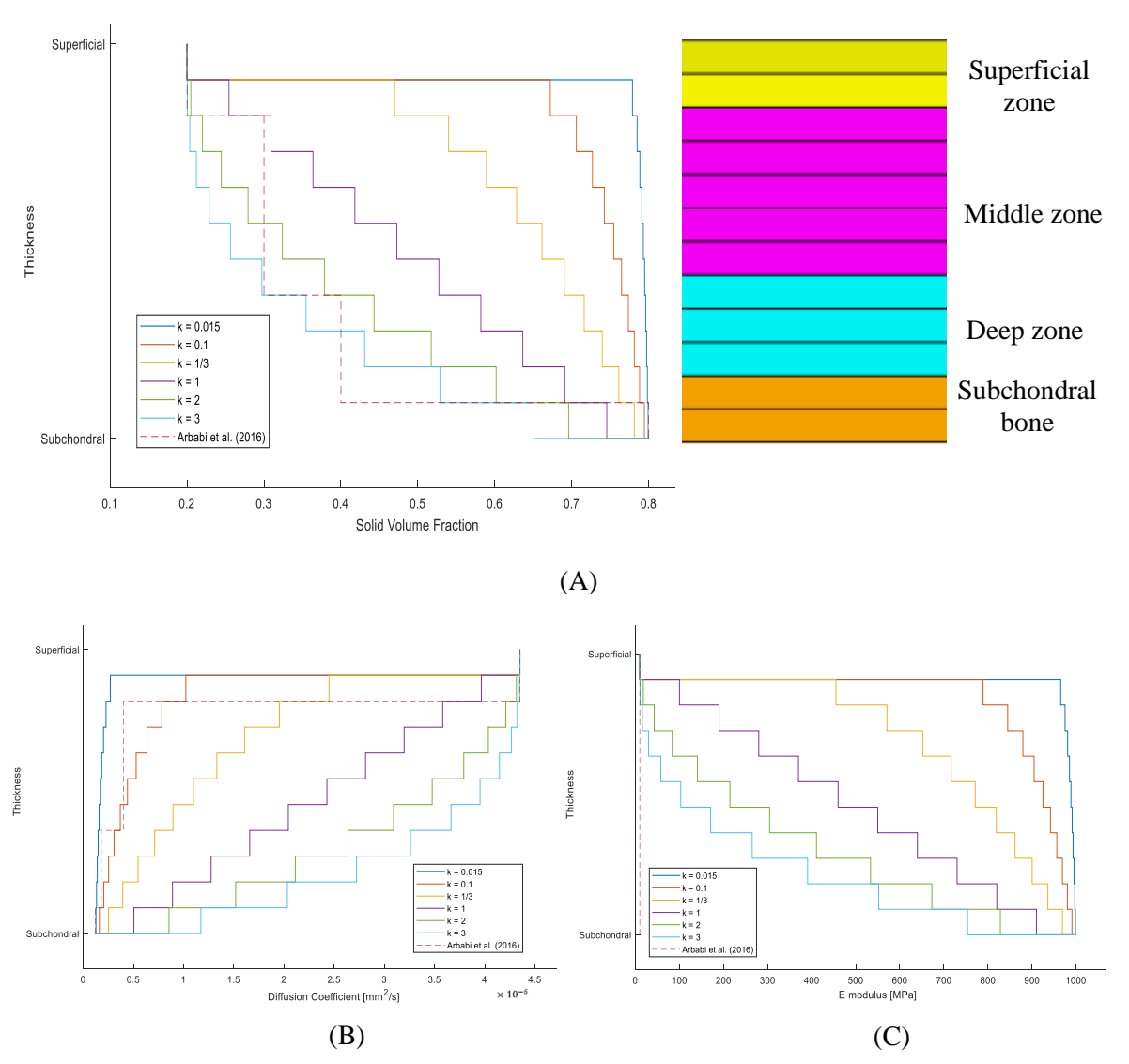


Figure 2.3: Plots of the values of the solid volume fraction (A), diffusion coefficient (B) and the elastic modulus (C) of each layer of the computational model as used in Arbabi et al. (2016) (dotted line), and for each used gradient k in equation 8.

## 2.1.3 Initial and Boundary Conditions

The initial solute concentration in the bath was taken 420 mM, corresponding to the solute concentration used in the diffusion experiment of Arbabi et al. (2015). To ensure that the effective solute pressure  $(\tilde{p})$  is continuous across boundaries (Ateshian et al., 2011), the following equation was used:

$$\tilde{p} = p - R\theta \phi, \tag{9}$$

where  $p=101\,kPa$ ,  $R=8.314e^{-6}{\rm mJ/nmol}\cdot K$ ,  $\theta=298\,K$ , and  $\phi=1$  (Arbabi et al., 2015, 2016).

#### 2.1.4 Validation

To validate the mesh refinement of the computational model, the initial parameter values of the model of Arbabi et al. (2016) were copied and simulated for 72 hours. The resulting concentration-time data of the HAC was compared with the experimental data found by Arbabi et al. (2016) by calculating the root mean square error (RMSE) between these two datasets. For the SCB layer, the RMSE was calculated between the experimental (Arbabi et al. (2016), and computational equilibrium concentration in the SCB. Both the RMSE of the HAC, and the SCB found by the computational model of this study were compared to the RMSE values for the HAC, and SCB obtained by the computational model of Arbabi et al. (2016).

#### 2.1.5 Near-Equilibrium Concentration Time

A MATLAB (2023b) code (Appendix B) was written that simultaneously runs the simulations in FEBio for the selected values of k on the SVF of the osteochondral model and plots the concentration-time curves to find the near-equilibrium concentration time point in the SCB. Likewise, two additional MATLAB codes were written, one applied the selected gradients k on the diffusion coefficient values of the OC model, and the latter applied the selected gradients k on the E modulus values of the OC model. In all three MATLAB codes, the concentration was normalized for the height of the SCB and each simulation was run until the near-equilibrium concentration in the SCB was reached. The near-equilibrium concentration time was found when a slope of less than 0.001 was obtained between two time points.

# 2.2 Diffusion Experiments

#### 2.2.1 Sample Preparation

An extrusion-based 3D-printer (BIO X, Cellink, Sweden) was used to print cylindrical hydrogel plugs (height = 2.4 mm). The ink used was a thermosensitive, ready-to-use, porcine gelatine-based GelMA (Cellink, Sweden) and extruded with a temperature of 32 °C on a cold petri dish (15 °C) with a pressure of 10 kPa and crosslinked with UVA (364 nm) light with a source-sample distance of 3 cm. The samples were printed inside cylindrical tubes with an inner diameter of 12.36 mm and a height of 9.8mm. The cylindrical tubes were obtained by cutting and polishing syringes (Fisherbrand, Fisher Scientific, U.S.A.) (Figure 2.4). To overcome the height of the cylindrical tubes, a one-inch (2.54 cm) long dispensing tip (Vieweg, Germany) with an inner diameter of 0.25 mm was used to extrude the GelMA in the tubes. The horizontal spacing between the path of the extruder was held constant at 0.5 mm (Figure 2.5A). This way, with the applied pressure, the extruded hydrogel filled the whole area and no empty spaces were left behind. Each printed layer had a height of 0.2 mm, so a total of

12 layers have been printed to obtain a total height of 2.4 mm (Figure 2.5B). Knowing that the SZ/MZ/DZ comprise 20/50/30% of the cartilage thickness (Sophia Fox et al., 2009), the total number of layers for each zone were 2, 5, 3, and 2 for the SZ, MZ, DZ, and SCB, respectively (Figure 2.5B).

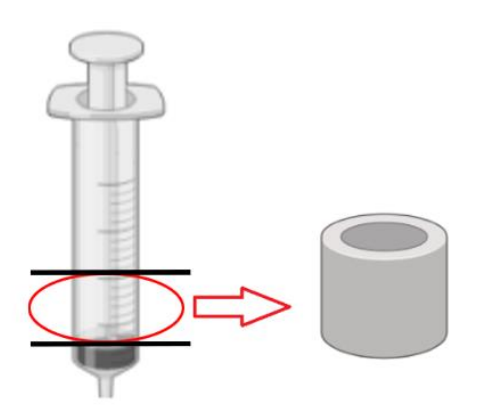
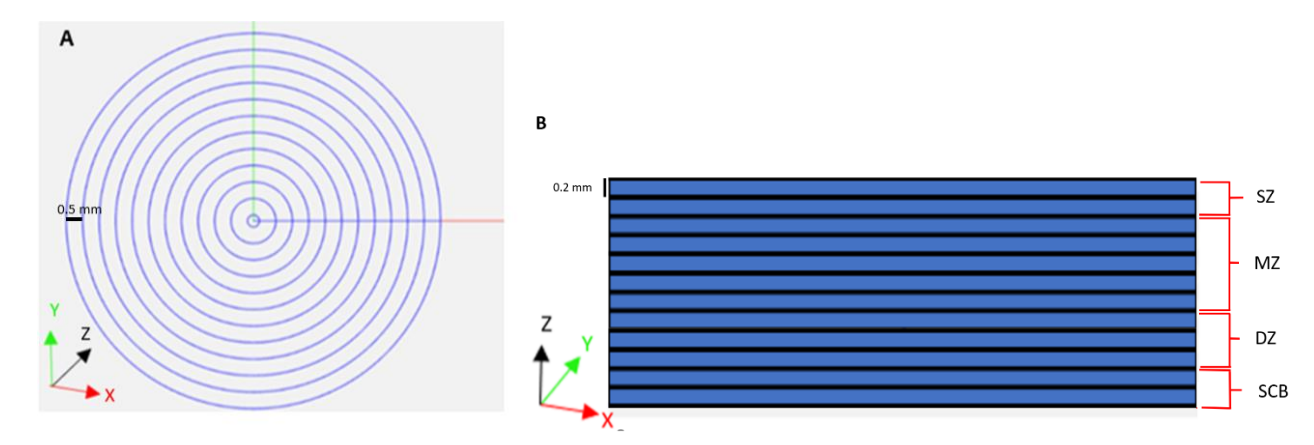


Figure 2.4: Cylindrical tubes were obtained from syringes.



*Figure 2.5:* (A) Horizontal view of the trajectory of the extruder, the spacing between the paths is held constant at 0.5 mm. (B) Illustrative picture of the frontal plane of the printed hydrogel plugs. Each plug was comprised of 12 layers, each 0.2 mm high.

Several attempts have been made to 3D-print the hydrogel samples using the protocol as described in the section above, only variating the extrusion temperature and pressure. Unfortunately, no successful prints could be accomplished, mostly because the GelMA solidified prematurely within the inch-long dispensing tip or was too viscous which results in over-extrusion of the GelMA and a poor resolution of the printed samples. Therefore, it was decided to cast droplets of GelMA in the cylindrical tubes to obtain hydrogel samples with a height of 2.4 mm. Because this method is not as accurate as 3D-printing, it was decided to prepare hydrogel plugs comprised of four layers of equal height (4 droplets per layer, representing 0.6 mm per layer).

An increased photocuring time of GelMA leads to a higher E modulus and a more dense ECM (and therefore higher SVF) (Miri et al., 2018). Hence, a lower diffusion coefficient for the GelMA is

expected if the photocuring time increases. By changing the photocuring time, 15 hydrogel plugs were created and subdivided into five groups (Table 2.2). Four of the five groups underwent a homogeneous photocuring time for the whole sample (45, 90, 180, or 300 seconds), where the photocuring time of the fifth (graded) group was graded over the height of the samples (Table 2.2, Figure 2.6). To print the graded samples, the first four droplets of GelMA representing the SCB layer were put in the tube and photocured for 120 s, then the GelMA representing the DZ was put in the tube and both the SCB and DZ were photocured for 90 s, followed by adding the MZ layer and photocuring the SCB, DZ and MZ for 45 s. Finally, the GelMA representing the SZ was added on top of the MZ, whereafter the whole sample was photocured for 45 s, such that the total amount of photocuring time for each layer was 300/180/90/45 seconds for the layers representing the SCB/DZ/MZ/SZ, respectively (Figure 2.6).

Table 2.2: Grouping of the printed hydrogel samples with their corresponding total UV curing time.

| Group              | No. of samples | UV curing time          |  |  |  |
|--------------------|----------------|-------------------------|--|--|--|
| Homogeneous UV 45  | 3              | 45s                     |  |  |  |
| Homogeneous UV 90  | 3              | 90s                     |  |  |  |
| Homogeneous UV 180 | 3              | 180s                    |  |  |  |
| Homogeneous UV 300 | 3              | 300s                    |  |  |  |
| Graded             | 3              | Combined (total = 300s) |  |  |  |

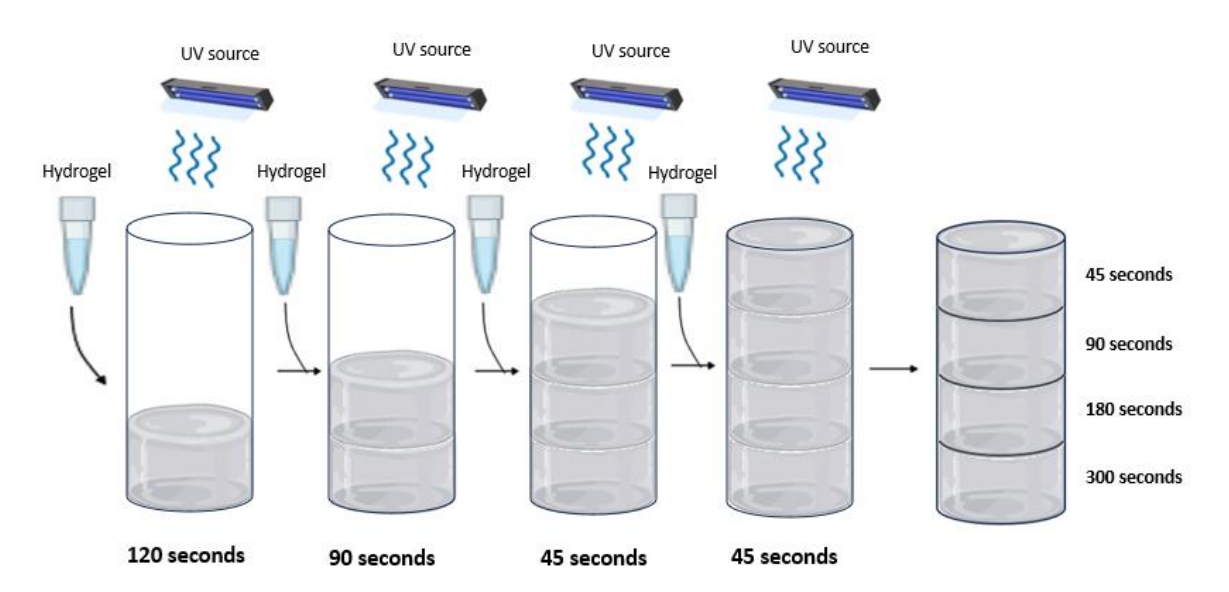


*Figure 2.6*: Schematic drawings showing the fabrication of the graded hydrogel samples. The bottom layer is poured into the cylinder first and UV cured for 120 seconds. Then the second layer is poured on top of the first layer and the whole structure is UV cured for 90 seconds. Thereafter, the third layer is put into the cylinder and all three layers are UV cured for 45 seconds. Finally, the fourth layer is poured into the cylinder, whereafter the whole structure is UV cured for 45 seconds again.

### 2.2.2 Image Acquisition

Alizarin Red S (A3882, Sigma-Aldrich, U.S.A.) was diluted to 0.1% using distilled water. 0.6 mL of the solute was injected into the tubes on top of the hydrogel samples (corresponding to 0.5 cm bath height). The images used to measure the transport of the alizarin red solution through the hydrogel samples were acquired using a Sony A7R (with E 3.5/30 MACRO lens). Images were taken directly after putting the solution on top of the samples (t = 0), and every 10 minutes after t = 0 for 2 hours and 50 minutes (18 time points). The effect of fluctuating external light was minimized by placing a screen around the set-up (Figure 2.7).

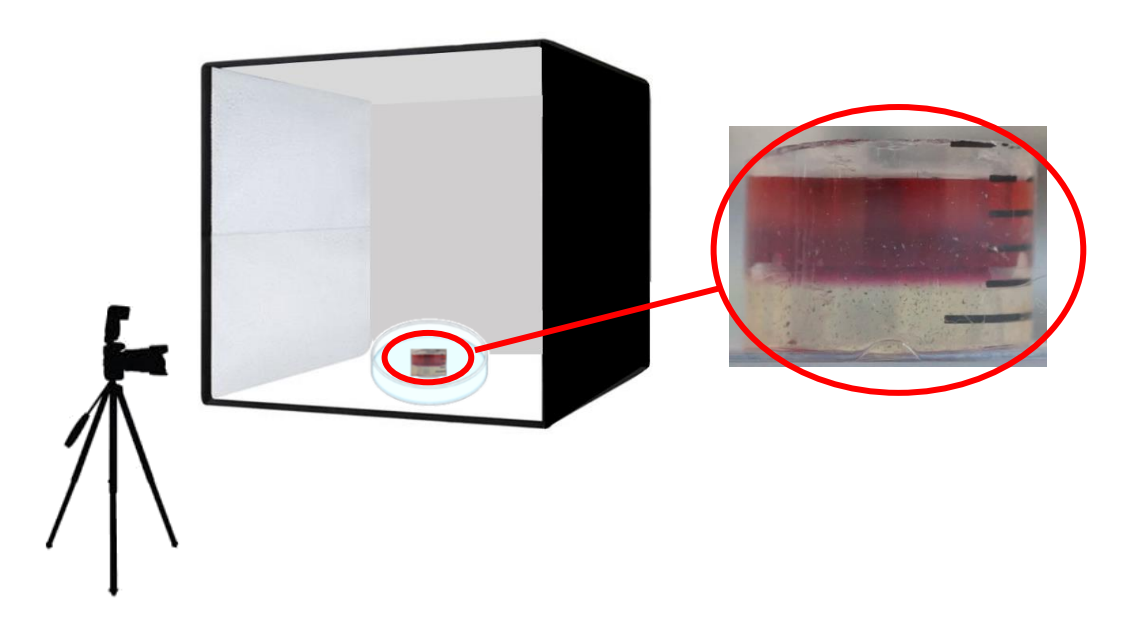


*Figure* 2.7: Experimental set-up of image acquisition, including a close-up of a sample at the start of the diffusion experiment showing alizarin red on top of the white hydrogel sample. A box is placed around the sample to minimize the effect of surrounding light on the samples during the diffusion experiment.

### 2.2.3 Image Processing

ImageJ (v1.51h) was used to process all the pictures. For each hydrogel, a rectangular region of interest (ROI) (width = 1.0 mm) containing all 12 layers of the hydrogel and a part of the bath, was selected and applied for every time point. Each of the prescribed ROIs was then subdivided into five separate ROIs representing the solute bath, SZ, MZ, DZ, and SCB. Thereafter for each image, the average grey value (Q) for each of the five ROIs was calculated with the following formula:

$$Q = \frac{\sum (P_i X_i)}{\sum (X_i)},$$

(10)

where  $P_i$  and  $X_i$  are the pixel intensity and pixel frequency, respectively.

Pouran et al. (2016) experimentally confirmed the existence of a linear relationship between the grey value of cartilage at t = 0 obtained from micro-CT images and the grey value of the bath at the same time point (eq. 11). This linear relationship was used to obtain the actual concentration of the solute inside the hydrogel.

$$C = \alpha Q + \beta, \tag{11}$$

where  ${\cal C}$  is the solute concentration,  $\alpha$  and  $\beta$  are constants, and  ${\cal Q}$  is the average grey value.

# 3 Results

# 3.1 Biphasic-Solute Model

#### 3.1.1 Validation of Refinement

Taking the initial parameter values of the model of Arbabi et al. (2016) for the computational model of this study, the RMSE for the cartilage was 0.1116, and for the SCB was 0.0001, which were almost identical to the RMSE values found by Arbabi et al. (2016) (0.1114 for the cartilage, and 0.0003 for the SCB) (Table 3.1).

**Table 3.1:** Root mean square error (RMSE) to compare the computational and experimental solute concentration versus time in cartilage and RMSE to compare the computational and experimental normalized equilibrium concentration in subchondral bone.

|  |      |                  | Arbabi et<br>al. (2016) | Mesh<br>refinement |  |  |
|--|------|------------------|-------------------------|--------------------|--|--|
|  |      | Cartilage        | 0.1114                  | 0.1116             |  |  |
|  | RMSE | Subchondral bone | 0.0003                  | 0.0001             |  |  |

## 3.1.2 Near-Equilibrium Concentration Time

By changing the gradient of the SVF, and diffusion coefficient values in the computational model, the near-equilibrium concentration time in the SCB was 1513.498 hours  $\pm$  256.8565 % (mean  $\pm$  SD) and 841.1847 hours  $\pm$  860.5269 % (mean  $\pm$  SD) for the SVF and diffusion coefficient models, respectively (Figure 3.1 & Figure 3.2). As for the model where gradients were applied on the E modulus, an average near-equilibrium concentration time for the solute in the SCB layer of 1260.999 hours  $\pm$  0.7925 % (mean  $\pm$  SD) is found (Figure 3.2).

The near-equilibrium concentration in the SCB for the SVF model was 95.9427 %  $\pm$  1.2445 % (mean  $\pm$  SD) (Figure 3.1). The near-equilibrium concentration in the SCB for the diffusion coefficient, and E modulus models were 94.7033 %  $\pm$  0.1664 % (mean  $\pm$  SD), and 94.6533 %  $\pm$  0.0003 % (mean  $\pm$  SD), respectively (Figure 3.2). Figure 3.3 shows the trend of the near-equilibrium concentration time against k of the SVF-, diffusion coefficient-, and E modulus model.

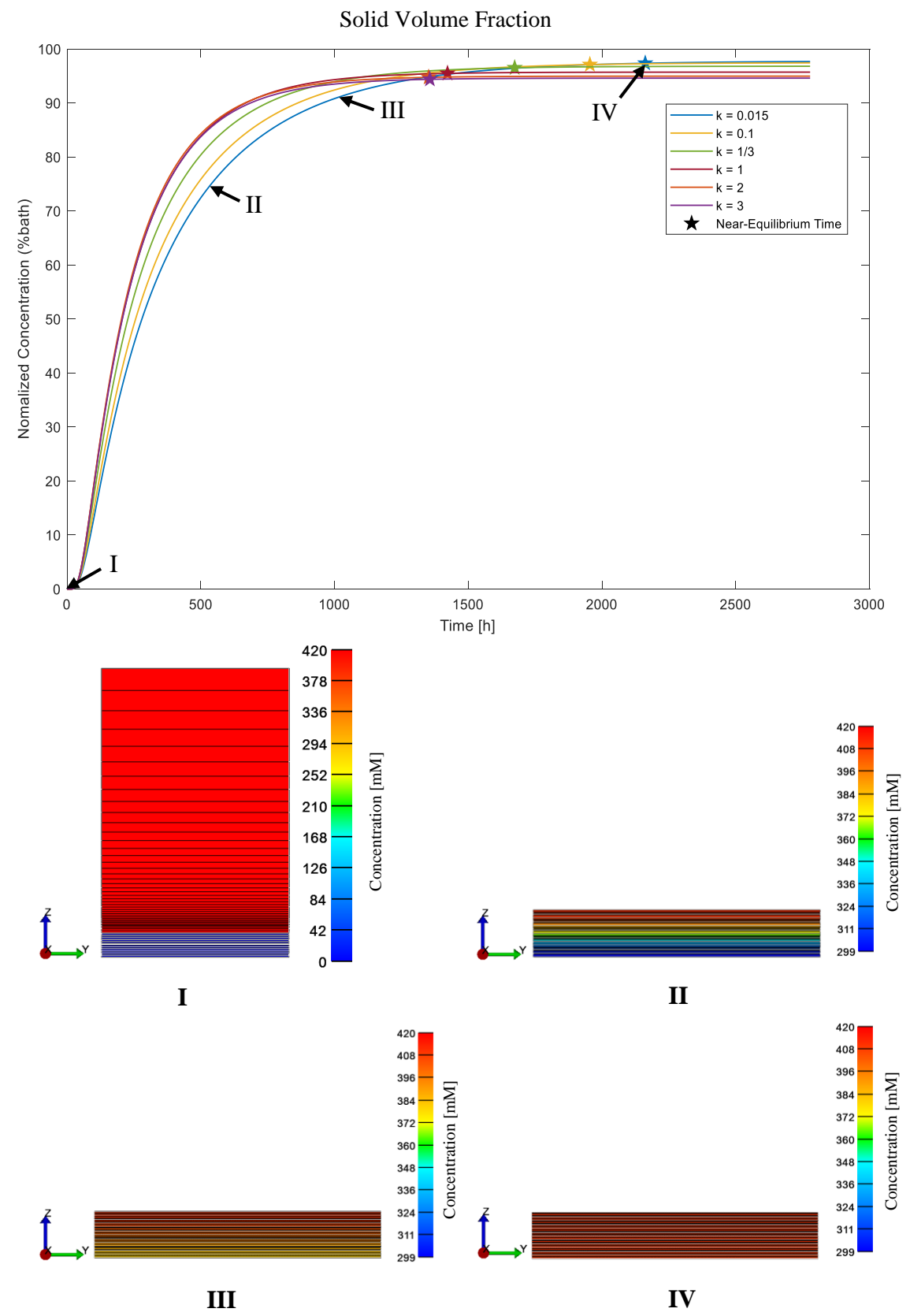
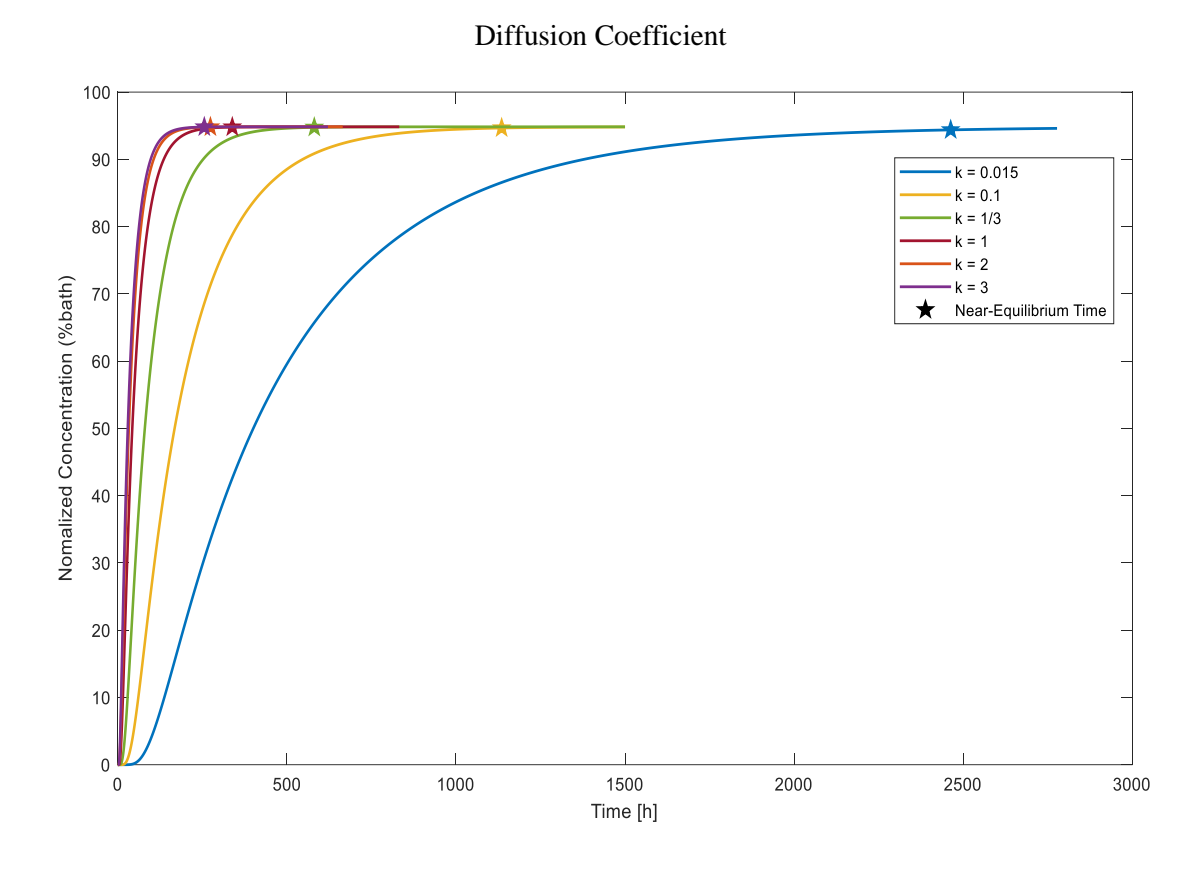
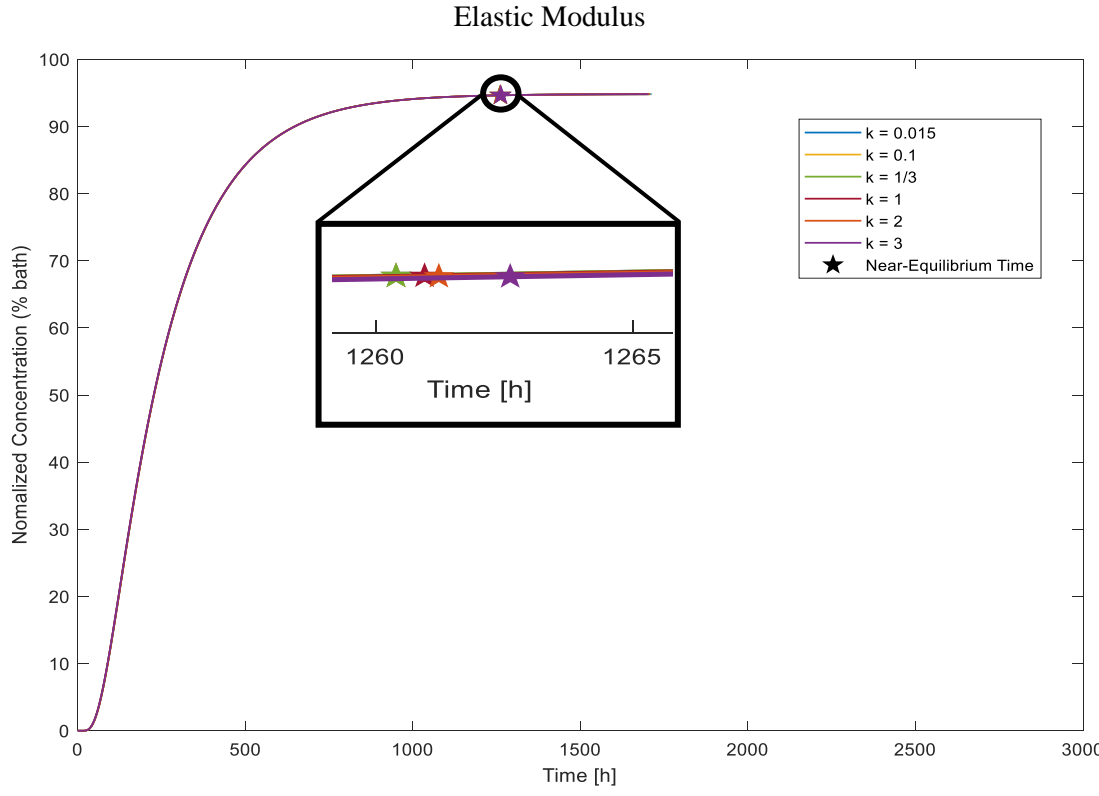
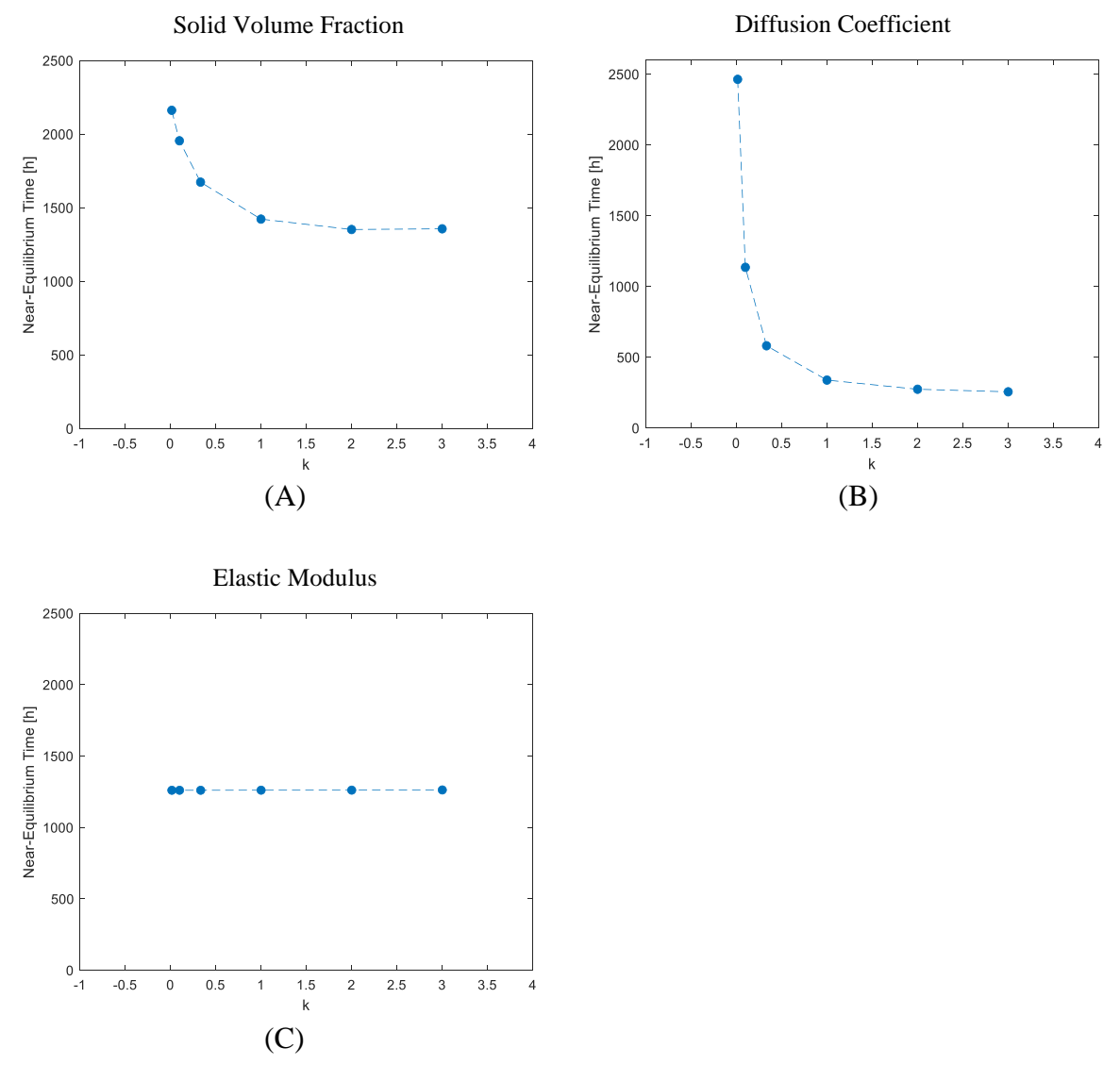


Figure 3.1: Plot of the normalized solute concentration in the subchondral plate against time for different gradients k applied on the solid volume fraction of the computational model, and their corresponding near-equilibrium time points (stars). The distribution of the solute concentration within the osteochondral model and solute bath at t=0 is shown in I. The distribution of the solute concentration in the osteochondral model for when k=0.015 is applied on the solid volume fraction at  $t=500,\,1000,\,$  and 2161 hours is shown in II, III, and IV, respectively.





*Figure 3.2:* Simulated normalized concentration against time for the subchondral plate for different values of *k* on the solid volume fraction (top graph) and diffusion coefficient (bottom graph), and their corresponding near-equilibrium concentration time points (stars).



*Figure 3.3:* Near-equilibrium concentration time plotted against gradient *k* applied on the solid volume fraction (A), diffusion coefficient (B), and the elastic modulus (C) values of the computational model.

# 3.2 Diffusion Experiments

Despite being careful, still, the moulded hydrogel plugs had different heights (Table 3.2). Figure 3.4 shows the diffusion of the solute through sample 'homogeneous UV90 #2' at the start (t = 0), t = 50 minutes, t = 110 minutes, and t = end (170 minutes). Air bubbles and/or sincere light reflections in/on the hydrogel samples during the diffusion experiments made most of the obtained data unusable. Leakage of the alizarin red solution between the hydrogel and cylindrical holder occurred with one sample (homogeneous UV300 #2), making this sample unsuitable for further analysis (Figure 3.5). After critical evaluation, only six samples (UV45 #1, UV45 #2, UV90 # 2, UV180 #2, UV300 #1, and Graded #2) were selected for further examination.

Only the samples that were homogeneously UV cured for 180 and 300 seconds reached an equilibrium concentration in the SCB zone, namely 65.32 % and 79.03 %, respectively (Figure 3.6). Low sample thickness is a factor contributing to the diffusion (Table 3.2, Figure 3.6).

Table 3.2: Total thickness of the hydrogel samples.

|        | Homogeneous UV 45 |      |       | Homogeneous UV 90 |       | Homogeneous UV 180 |      | Homogeneous UV 300 |       |       | Graded |       |       |       |      |
|--------|-------------------|------|-------|-------------------|-------|--------------------|------|--------------------|-------|-------|--------|-------|-------|-------|------|
|        | 1                 | 2    | 3     | 1                 | 2     | 3                  | 1    | 2                  | 3     | 1     | 2      | 3     | 1     | 2     | 3    |
| Height | 4.05              | 2.82 | 2.035 | 2.755             | 2.376 | 2.812              | 2.42 | 2.401              | 2.032 | 1.554 | 2.486  | 1.015 | 4.033 | 2.844 | 0.93 |
| (mm)   | 1.03              | 2.02 | 2.033 | 2.733             | 2.570 | 2.012              | 2.12 | 2.101              | 2.032 | 1.55  | 2.100  | 1.015 | 1.055 | 2.011 | 0.55 |

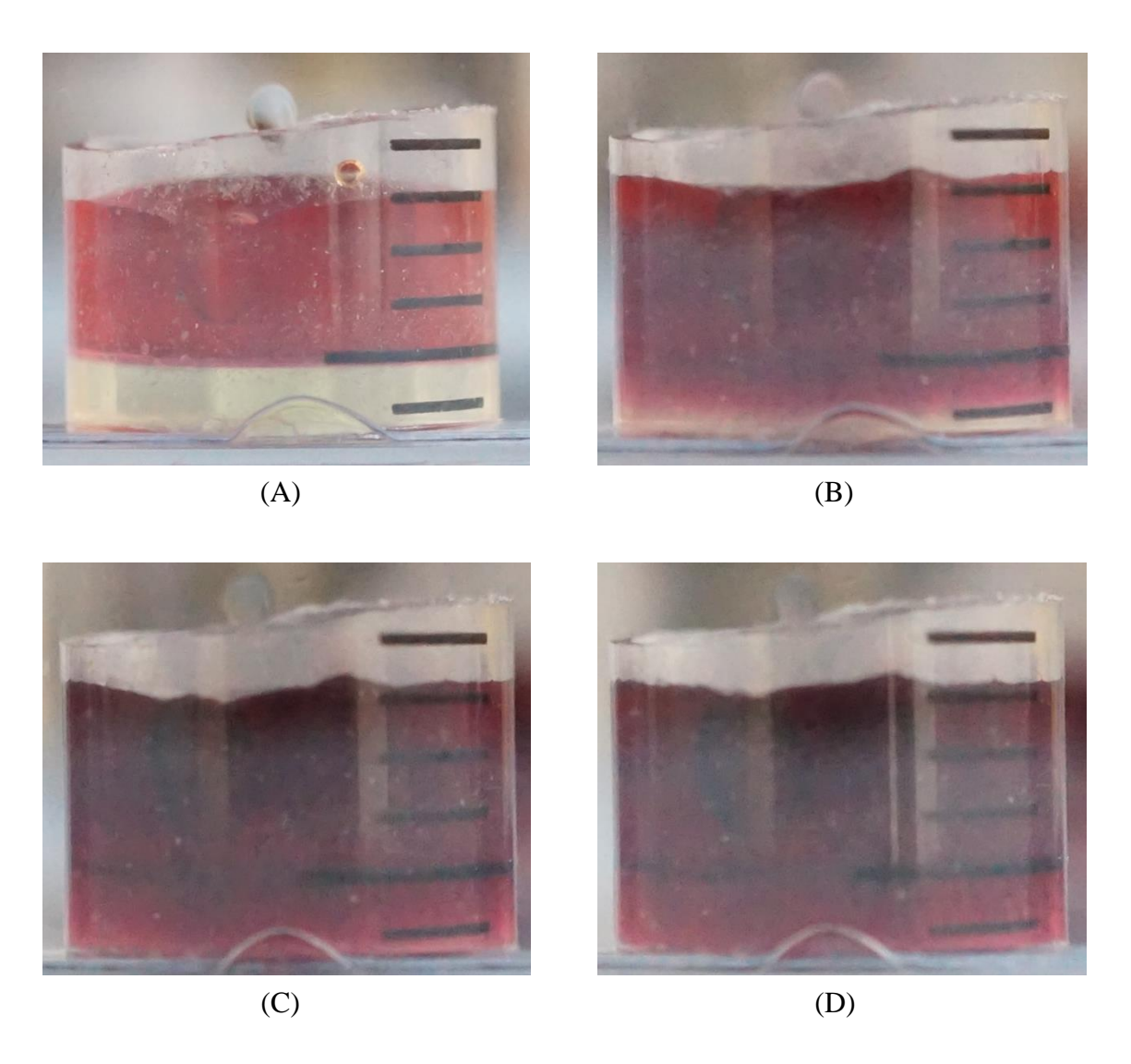
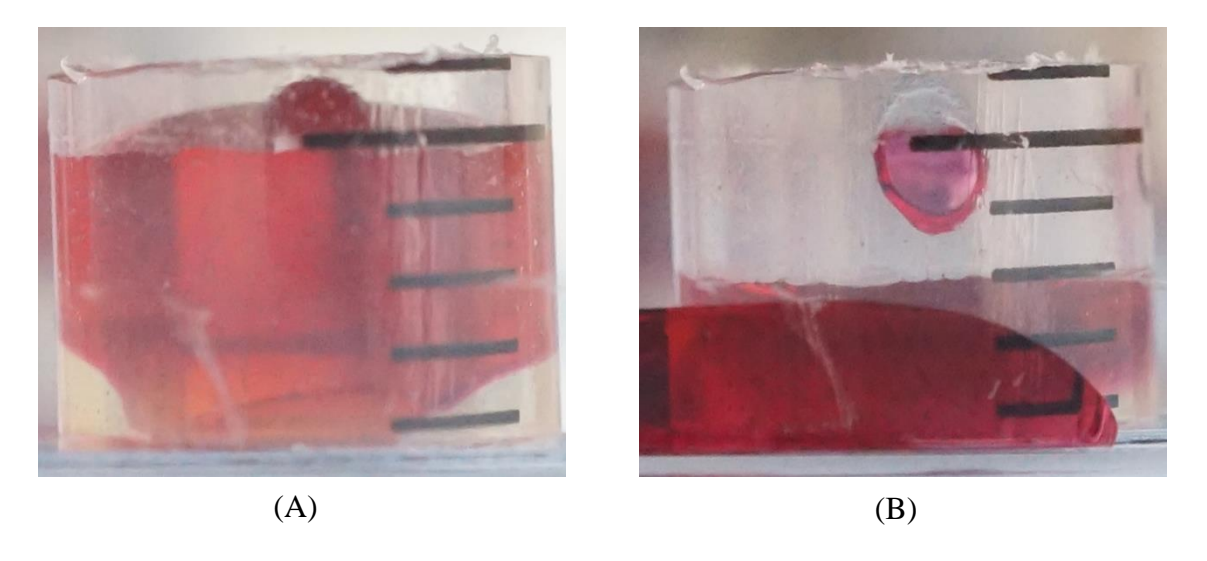
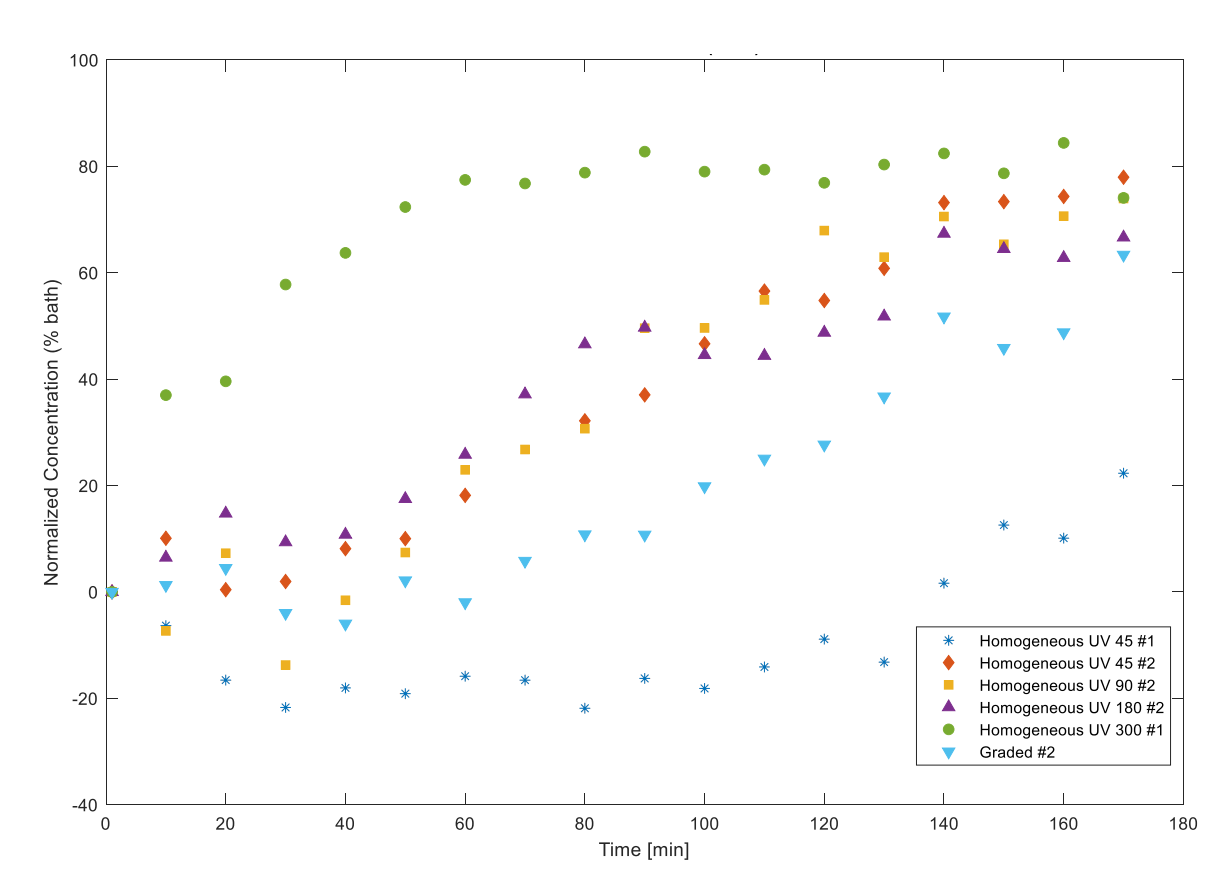


Figure 3.4: Images of hydrogel sample 'Homogeneous UV90 #2' during the diffusion experiment at t = 0 (A), t = 50 minutes (B), t = 110 minutes (C), and the end of the experiment t = 170 minutes (D).



*Figure 3.5:* Images of homogeneous UV300 #2 at t = 0 (A) and t = 20 minutes (B), showing leakage of the alizarin red solution between the hydrogel sample and cylindrical plug.



*Figure 3.6:* Normalized concentration of alizarin red solution in the subchondral layer of the hydrogel samples against time.

# 4 Discussion

The aim of this master's thesis was to investigate how graded mechanical- and/or physiological properties of the OC interface affect the solute transport across the OC interface. A computational model that accurately replicates the diffusive behaviour of the OC interface was designed and used to obtain the relationship between different gradients for the SVF, diffusion coefficient and E modulus through the OC interface and the solute transport across the OC interface. Furthermore, diffusion experiments were performed on GelMA-based hydrogel plugs to investigate the relationship between UV crosslinking time and solute transport through GelMA.

# 4.1 Biphasic-Solute Model

The RMSE values for cartilage and the SCB plate obtained by our computational model (0.1116 and 0.0001, respectively) are highly comparable to the RMSE values for cartilage and SCB (0.1114 and 0.0003, respectively) found by the validated model of Arbabi et al. (2016) (Table 3.1), thereby validating the computational model of this master's thesis for the parameter values of Arbabi et al. (2016). It should be noted that the micro-CT experiments in the study of Arbabi et al. (2016) failed to distinguish calcified cartilage from SCB. Therefore, the models did not include the naturally occurring calcified cartilage layer. Furthermore, the near-equilibrium concentration-time points found for the SCB actually represent the time when near-equilibrium concentration is reached within the whole unit of calcified cartilage and SCB.

Changing the gradient of the values for SVF across the OC interface had a lesser effect on the near-equilibrium concentration time compared to changing the gradient of the diffusion coefficient, but was still substantial (Figure 3.3A & Figure 3.3B). Whereas changing the gradient of the E modulus values across the OC interface had a negligible effect on the near-equilibrium concentration time (Figure 3.3C). A lower water content (higher SVF) throughout the OC interface appears to increase the equilibrium concentration of the solute in the SCB (Figure 2.3 and Figure 3.1). Moreover, a higher SVF throughout the OC interface increases the near-equilibrium concentration time in the SCB (Figure 2.3 and Figure 3.3). This is in accordance with the studies of Lotke & Granda (1971, 1972), which indicated that the solid proteoglycan molecules acted as a solute filter and the main constraint to solute transport. Thus, a higher SVF provides more resistance for the solute transport through the material, thereby resulting in a longer time to reach the equilibrium concentration. As for the SVF, a lower value of k for the diffusion coefficient provides a higher near-equilibrium

concentration time (Figure 3.2). However, it is needed to say that all of the findings in this paragraph are not validated since a computational model could only be validated by data from *in vivo* and *in vitro* experiments which could be obtained from either literature or purposely designed studies (Viceconti et al., 2005) and none was obtained.

The solute used in the models was electrically neutral, allowing that the effects of fixed charges in the OC interface, and the resulting electromechanically created diffusion, could be ruled out. Consequently, the molecular friction between the solute and the ECM of the cartilage (being SVF, collagen fibrils, and proteoglycans) and the morphology of the SCB (thickness and porosity) are the only constraining factors for neutral solute diffusion through the OC interface. Suggesting that the diffusion in this master's thesis could be described as a Fickean diffusion process. A limitation of the model is that the geometry is simplified by flat, uniform layers, whereas the natural OC interface has an irregular curvature and variating thickness for HAC and SCB within the joint. Furthermore, the thickness of the different zones of cartilage are divided by 20/50/30% of the total cartilage height for the SZ/MZ/DZ, respectively. However, the distribution of the articular cartilage zones is not set at exactly these percentages and could differ between joints and is even location dependent within a joint (Bullough & Goodfellow, 1968; Clark, 1985).

Another limitation of this master's thesis is that only axial diffusion was assumed in the model. However, it is known that the diffusion tensor is anisotropic (Leddy & Guilak, 2008), which could cause diffusion patterns in radial and/or tangential directions that are not taken into account by axial models. The size of the solute molecules in the computational model is comparable with some molecules that are important for cartilage metabolism (Ameye & Chee, 2006; Schadow et al., 2013), but relatively small compared to the greater part of the relevant molecules (Didomenico et al., 2018). Given that the size of the relevant molecules could vary significantly and that the molecular size affects the diffusion rate, it is impossible that the full range of all relevant molecules could be represented by a single molecule. However, the effect of the studied graded parameters on the diffusion rate through the OC interface is shown in this master's thesis. Despite the fact that the absolute diffusion rate might be different for different molecule sizes, the main finding of this master's thesis, that a lower k for both the SVF and diffusion coefficient provides a higher near-equilibrium concentration time and that the E modulus does not affect the molecular diffusion across the OC interface, is expected to hold no matter what the size of the molecule is.

# 4.2 Experiments

#### 4.2.1 3D-Printing

As mentioned before, several attempts were made to 3D-print the hydrogel samples using the protocol as described in section 2.2.1 as a starting point, variating the extrusion temperature and pressure. Unfortunately, no successful prints could be made using the current set-up, mostly because the GelMA solidified prematurely within the inch-long dispensing tip or was too viscous which results in over-extrusion of the GelMA and a poor resolution of the printed samples. The limited range of GelMA concentrations that allows for the extrusion of the hydrogel is a known limitation for 3D-printing GelMA with a nozzle or syringe (Bertassoni et al., 2014; Hölzl et al., 2016; Pepelanova et al., 2018). Removing the inch-long needle would generally expand the range of printable GelMA concentrations due to the smaller distance between the nozzle and the printing surface (Naghieh & Chen, 2021). However, in this master's thesis, the height of the cylindrical tubes must be overcome, making the inch-long needle essential in the current set-up. Ideas of how to improve the current set-up are presented later on in the recommendations section (Chapter 4.3).

#### 4.2.2 Diffusion Experiments

After a time period of two hours and 50 minutes, only the evaluated hydrogel samples that are homogeneously UV cured for 180 and 300 seconds reached an equilibrium concentration in the SCB layer (Figure 3.6). Looking at the graph shown in Figure 3.6, homogeneously cured samples UV45 #2 and UV90 #2 appear to have almost reached the equilibrium concentration. It is observed that sample thickness is a factor contributing to the diffusion rate (Table 3.2, Figure 3.6). Noteworthy is that samples UV45 #1, UV90 #2, and Graded #2 had multiple time points with a negative concentration in the SCB zone, some even up to -20% of the bath concentration. Most likely, these negative values occurred because light reflections sincerely influenced the average grey value(-s) at t = 0 and/or at the time(-s) the negative concentration is calculated since the concentration is calculated directly from the average grey value.

Looking at the analysed samples with comparable height (UV45 #2 and Graded #2, and UV90 #2 and UV180 #2), the trend of the solute concentration in the SCB zone between UV90 #2 and UV180 #2 is pretty similar apart from that the equilibrium concentration tends to be lower for the sample with a longer UV curing time (Figure 3.6). However, looking at the samples with a bigger difference in UV curing time (UV45 #2 and Graded #2), the solute concentration in the SCB zone seems to increase quicker in the sample with a shorter UV

curing time (Figure 3.6). A longer UV curing time causes more polymers to be crosslinked, thereby creating a more dense structure which accompanies a higher SVF and E modulus (Bertassoni et al., 2014). Comparing these two findings with the results of our computational model where only the gradient of the SVF is changed (Figure 3.1), we note that the near-equilibrium concentration in the simulations with a lower overall SVF (simulations with a higher k value) is lower than the near-equilibrium concentration of simulations with a higher overall SVF, contradicting the experimental finding that the equilibrium concentration in the SCB layer is lower for the samples with a longer UV curing time (Figure 3.6). However, the simulations of the computational model also suggest that the concentration in simulations with a lower overall SVF (simulations with a higher k) increases quicker than the concentration of the simulations with a higher overall SVF, which is in line with the experimental diffusion test. However, it is necessary to mention that, apart from the relationship between sample thickness and diffusion rate, no conclusions could be drawn from the diffusion experiments due to the fact the diffusion time period was set too brief to reach an equilibrium concentration in most cases and because only a few samples were available for data analysing due to the exclusion of most samples because of sincere light reflections and/or air bubbles. Looking at Figure 3.6, adding two more hours to the diffusion experiment most likely will result that the concentration in the SCB layer of hydrogel samples with a height of 2.4 mm will reach to an equilibrium.

One of the limitations of the current set-up is that the data is collected using a digital camera, which is only able to record the outer surface of the sample in 2D. As a consequence, the camera is not able to distinguish whether the alizarin red diffuses through the hydrogel sample or is running down along the sample instead. It is therefore of crucial importance that there is no space between the hydrogel sample and the cylindrical holder such that the solute could not run down along the hydrogel. Furthermore, light reflections from the surrounding area could influence the average grey value of the images from the outer surface. As mentioned before, the solute concentration is calculated using the average grey value. Therefore, the light reflections could bias the results if they do not cover the whole sample. Recommendations on how to improve the current experimental set-up will be discussed in the following subchapter.

## 4.3 Recommendations

From the results and discussion, a set of recommendations is formulated for further research. The first recommendation will be to accurately identify the thickness of the cartilage zones and SCB layer

of the studied OC sample first and then implement this in the computational model. This way, the model replicates the geometry of the OC sample more accurately.

As mentioned before, the budget and time span for this master's thesis were not unlimited. For future diffusion-related studies using GelMA-based hydrogel samples with the same height as used in this master's thesis, a longer diffusion time is recommended to ensure that the equilibrium concentration will be reached. As mentioned earlier, looking at Figure 3.6, adding two more hours to the diffusion experiment will most likely be sufficient to reach an equilibrium concentration in the SCB layer of 2.4 mm high hydrogel samples.

The current set-up uses a digital camera which obtains 2D images of the outer surface. For future research, it is recommended to use 3D-imaging techniques, like micro-CT, instead. 3D-imaging techniques allow for the examination of the solute diffusion over time across, for example, the mid-coronal slice of the GelMA samples. This overcomes the influence of external light on the grey values of the images which is a major drawback of the digital camera used in the current set-up. Moreover, with 3D-imaging techniques, the tube which the GelMA is poured into no longer needs to be transparent in order to be able to capture the solute diffusion across the hydrogel with the camera, increasing the number of materials available that could be used for the cylindrical holder. Some of the newly available materials could have the ability to shrink and make a perfect fit around the hydrogel sample. This way, the GelMA does not need to be poured directly into the cylindrical tube, making the inch-long needle in 3D-printing unnecessary, and therefore, increasing the printability of the GelMA. If, however, a 2D-imaging technique is used to obtain the solute diffusion, it is recommended to fabricate more GelMA samples so that, despite the loss of samples due to light reflections, air bubbles, or leakages, there are still enough samples left for analysing.

## 5 Conclusion

This master's thesis aimed to investigate how graded mechanical- and/or physiological properties of the OC interface affect the solute transport across the OC interface. A computational model that accurately replicates the diffusive behaviour of a neutral solute across the OC interface was designed and used to obtain the relationship of different gradients for the SVF, diffusion coefficient and E modulus through the OC interface and the solute transport across the OC interface. Furthermore, diffusion experiments were performed on GelMA-based hydrogel plugs to investigate the relationship between UV crosslinking time and solute transport through GelMA.

From the results of the computational model, it is concluded that both the diffusion coefficient and SVF significantly influence the solute diffusion through the OC interface, whereas the E modulus has a negligible effect. Changing the gradient of the values for SVF across the OC interface has a lesser effect on the near-equilibrium concentration time compared to changing the gradient of the diffusion coefficient, but is still substantial. Regarding the SVF, a lower overall water content within the OC interface increases both the equilibrium concentration of the solute and the time until the solute equilibrium concentration is reached in the SCB. Like the SVF, a lower overall diffusion coefficient throughout the OC interface results in a higher equilibrium concentration time in the SCB than the simulations with an overall higher diffusion coefficient. However, unlike with the SVF, the diffusion coefficient does not really have an impact on the height of the equilibrium concentration of the solute in the SCB.

On the experimental side, using the current set-up, no successful 3D-printed GelMA plugs could be obtained due to the limited range of GelMA concentrations that allow for the accurate extrusion of GelMA by the 3D-printer. Using droplets of GelMA to produce hydrogel samples proved to be inadequate to obtain samples with the same height. The results of the hydrogel diffusion tests indicate a relation between sample thickness and the equilibrium concentration time, where a higher sample is accompanied by a longer time to reach the equilibrium concentration. Moreover, the diffusion experiments suggest that the solute concentration of GelMA samples with a longer UV curing time increases more rapidly and reaches a higher equilibrium than GelMA samples with a shorter UV curing time.

Comparing the results of the computational model and hydrogel diffusion tests, it looks like both are in agreement that the solute concentration in the SCB zone increases quicker when the overall

SVF is lower. However, the results of the diffusion experiments suggest that the near-equilibrium concentration in the SCB layer is lower for samples with a higher SVF. Thereby contradicting the results of the computational model which suggests that the equilibrium concentration in the SCB layer is lower when a higher overall SVF is present.

This master's thesis provides a new computational model of the OC interface that makes it possible to study the effect of graded parameters throughout the OC interface. New insights into how various gradients of the SVF, diffusion coefficient, and E modulus throughout the OC interface affect the solute diffusion through the OC interface are provided. However, more experimental data is needed to validate these findings which could lead to new repair strategies.

## **Bibliography**

- Ameye, L. G., & Chee, W. S. S. (2006). Research article Osteoarthritis and nutrition. From nutraceuticals to functional foods: a systematic review of the scientific evidence. *Arthritis Research & Therapy*, 8(4), 1–22. https://doi.org/10.1186/ar2016
- Ansari, S., Khorshidi, S., & Karkhaneh, A. (2019). Engineering of gradient osteochondral tissue: From nature to lab. *Acta Biomaterialia*, 87, 41–54. https://doi.org/10.1016/j.actbio.2019.01.071
- Antons, J., Marascio, M. G. M., Nohava, J., Martin, R., Applegate, L. A., Bourban, P. E., & Pioletti, D. P. (2018). Zone-dependent mechanical properties of human articular cartilage obtained by indentation measurements. *Journal of Materials Science: Materials in Medicine*, 29(5), 57. https://doi.org/10.1007/s10856-018-6066-0
- Arbabi, V., Pouran, B., Weinans, H., & Zadpoor, A. A. (2015). Transport of Neutral Solute Across Articular Cartilage: The Role of Zonal Diffusivities. *Journal of Biomechanical Engineering*, 137(7).
- Arbabi, V., Pouran, B., Weinans, H., & Zadpoor, A. A. (2016). Neutral solute transport across osteochondral interface: A finite element approach. *Journal of Biomechanics*, 49(16), 3833–3839.
- Ateshian, G. A., Albro, M. B., Maas, S., & Weiss, J. A. (2011). Finite Element Implementation of Mechanochemical Phenomena in Neutral Deformable Porous Media Under Finite Deformation. *Journal of Biomechanical Engineering*, *133*(8). https://doi.org/10.1115/1.4004810
- Ateshian, G. A., Maas, S., & Weiss, J. A. (2012). Solute Transport Across a Contact Interface in Deformable Porous Media. *Journal of Biomechanics*, 45(6), 1023–1027. https://doi.org/10.1016/j.jbiomech.2012.01.003
- Ateshian, G. A., & Weiss, J. A. (2013). Finite element modeling of solutes in hydrated deformable biological tissues. In *From Nano to Macro* (pp. 231–249). Springer Netherlands.
- Bernstein, A., Niemeyer, P., Salzmann, G., Südkamp, N. P., Hube, R., Klehm, J., Menzel, M., Von Eisenhart-Rothe, R., Bohner, M., Görz, L., & Mayr, H. O. (2013). Microporous calcium phosphate ceramics as tissue engineering scaffolds for the repair of osteochondral defects: Histological results. *Acta Biomaterialia*, *9*(7), 7490–7505. https://doi.org/10.1016/j.actbio.2013.03.021
- Bertassoni, L. E., Cardoso, J. C., Manoharan, V., Cristino, A. L., Bhise, N. S., Araujo, W. A., Zorlutuna, P., Vrana, N. E., Ghaemmaghami, A. M., Dokmeci, M. R., & Khademhosseini, A. (2014). Direct-write bioprinting of cell-laden methacrylated gelatin hydrogels. *Biofabrication*, 6(2), 024105.
- Bhosale, A. M., & Richardson, J. B. (2008). Articular cartilage: Structure, injuries and review of management. *British Medical Bulletin*, 87(1), 77–95. https://doi.org/10.1093/bmb/ldn025
- Botter, S. M., Van Osch, G. J. V. M., Clockaerts, S., Waarsing, J. H., Weinans, H., & Van Leeuwen, J. (2011). Osteoarthritis induction leads to early and temporal subchondral plate porosity in the tibial plateau of mice: An in vivo microfocal computed tomography study. *Arthritis and Rheumatism*, 63(9), 2690–2699. https://doi.org/10.1002/art.30307
- Broom, N. D., & Thambyah, A. (2018). The Osteochondral Junction. In *The Soft–Hard Tissue Junction: Structure, Mechanics, and Function*. https://doi.org/10.1017/9781316481042.003
- Brown, T. D., Radin, E. L., Martin, R. B., & Burr, D. B. (1984). Finite element studies of

- some juxtarticular stress changes due to localized subchondral stiffening. *Journal of Biomechanics*, 17(1), 11–24. https://doi.org/10.1016/0021-9290(84)90075-7
- Buckwalter, J. A., & Mankin, H. J. (1997). Articular cartilage. Part I: Tissue design and chondrocyte-matrix interactions. *Journal of Bone and Joint Surgery Series A*, 79(4), 600–611.
- Buckwalter, J. A., & Mankin, H. J. (1998). Articular cartilage: degeneration and osteoarthritis, repair, regeneration, and transplantation. *Instructional Course Lectures*, 47, 487–504.
- Buckwalter, J. A., Mower, D., Ungar, R., Schaeffer, J., & Ginsberg, B. (1986). Morphometric analysis of chondrocyte hypertrophy. *Journal of Bone and Joint Surgery Series A*, 68(2), 243–255. https://doi.org/10.2106/00004623-198668020-00010
- Bullough, P., & Goodfellow, J. (1968). The significance of the fine structure of articular cartilage. *Journal of Bone and Joint Surgery Series B*, *50*(4), 852–857. https://doi.org/10.1302/0301-620X.50B4.852
- Burr, D. B., Schaffler, M. B., & Frederickson, R. G. (1988). Composition of the cement line and its possible mechanical role as a local interface in human compact bone. *Journal of Biomechanics*, 21(11), 939–945. https://doi.org/10.1016/0021-9290(88)90132-7
- Chakraborty, A., Gopalakrishnan, S., & Reddy, J. N. (2003). A new beam finite element for the analysis of functionally graded materials. *International Journal of Mechanical Sciences*, 45(3), 519–539. https://doi.org/10.1016/S0020-7403(03)00058-4
- Chen, L., Deng, C., Li, J., Yao, Q., Chang, J., Wang, L., & Wu, C. (2019). 3D printing of a lithium-calcium-silicate crystal bioscaffold with dual bioactivities for osteochondral interface reconstruction. *Biomaterials*, *196*, 138–150. https://doi.org/10.1016/j.biomaterials.2018.04.005
- Chen, Q., Zhu, C., & Thouas, G. A. (2012). Progress and challenges in biomaterials used for bone tissue engineering: bioactive glasses and elastomeric composites. *Progress in Biomaterials*, *I*(1), 2. https://doi.org/10.1186/2194-0517-1-2
- Choi, K., Kuhn, J. L., Ciarelli, M. J., & Goldstein, S. A. (1990). The elastic moduli of human subchondral trabecular and cortical bone tissue. *Journal of Biomechanics*, 23(11), 1103–1113. https://doi.org/10.1016/0021-9290(90)90003-L
- Clark, J. M. (1985). The organization of collagen in cryofractured rabbit articular cartilage: A scanning electron microscopic study. *Journal of Orthopaedic Research*, *3*(1), 17–29. https://doi.org/10.1002/jor.1100030102
- Clark, J. M. (1990). The structure of vascular channels in the subchondral plate. *Journal of Anatomy*, 171, 105–115.
- Cohen, N. P., Foster, R. J., & Mow, V. C. (1998). Composition and dynamics of articular cartilage: Structure, function, and maintaining healthy state. *Journal of Orthopaedic and Sports Physical Therapy*, 28(4), 203–215. https://doi.org/10.2519/jospt.1998.28.4.203
- Daly, A. C., Critchley, S. E., Rencsok, E. M., & Kelly, D. J. (2016). A comparison of different bioinks for 3D bioprinting of fibrocartilage and hyaline cartilage. *Biofabrication*, 8(4), 045002. https://doi.org/10.1088/1758-5090/8/4/045002
- Di Luca, A., Van Blitterswijk, C., & Moroni, L. (2015). The osteochondral interface as a gradient tissue: From development to the fabrication of gradient scaffolds for regenerative medicine. *Birth Defects Research Part C Embryo Today: Reviews*, 105(1), 34–52. https://doi.org/10.1002/bdrc.21092
- Di Martino, A., Kon, E., Perdisa, F., Sessa, A., Filardo, G., Neri, M. P., Bragonzoni, L., & Marcacci, M. (2015). Surgical treatment of early knee osteoarthritis with a cell-free

- osteochondral scaffold: Results at 24 months of follow-up. *Injury*, *46*, S33–S38. https://doi.org/10.1016/S0020-1383(15)30052-8
- Didomenico, C. D., Lintz, M., & Bonassar, L. J. (2018). Molecular transport in articular cartilage What have we learned from the past 50 years? *Nature Reviews Rheumatology*, *14*(7), 393–403. https://doi.org/10.1038/s41584-018-0033-5
- Doubrovski, E. L., Tsai, E. Y., Dikovsky, D., Geraedts, J. M. P., Herr, H., & Oxman, N. (2015). Voxel-based fabrication through material property mapping: A design method for bitmap printing. *CAD Computer Aided Design*, *60*, 3–13. https://doi.org/10.1016/j.cad.2014.05.010
- Duncan, H., Jundt, J., Riddle, J. M., Pitchford, W., & Christopherson, T. (1987). The tibial subchondral plate. A scanning electron microscopic study. *Journal of Bone and Joint Surgery Series A*, 69(8), 1212–1220. https://doi.org/10.2106/00004623-198769080-00015
- Dye, S. F., Vaupel, G. L., & Dye, C. C. (1998). Conscious Neurosensory Mapping of the Internal Structures of the Human Knee Without Intraarticular Anesthesia. *The American Journal of Sports Medicine*, 26(6), 773–777.
- Eltom, A., Zhong, G., & Muhammad, A. (2019). Scaffold Techniques and Designs in Tissue Engineering Functions and Purposes: A Review. *Advances in Materials Science and Engineering*, 2019. https://doi.org/10.1155/2019/3429527
- Fawns, H. T., & Landells, J. W. (1953). Histochemical studies of rheumatic conditions. I. Observations on the fine structures of the matrix of normal bone and cartilage. *Annals of the Rheumatic Diseases*, *12*(2), 105–113. https://doi.org/10.1136/ard.12.2.105
- Gilmore St., R. C., & Palfrey, A. J. (1987). A histological study of human femoral condylar articular cartilage. *Journal of Anatomy*, *155*, 77–85.
- Gupta, H. S., Schratter, S., Tesch, W., Roschger, P., Berzlanovich, A., Schoeberl, T., Klaushofer, K., & Fratzl, P. (2005). Two different correlations between nanoindentation modulus and mineral content in the bone-cartilage interface. *Journal of Structural Biology*, *149*(2), 138–148. https://doi.org/10.1016/j.jsb.2004.10.010
- Heinegård, D., & Oldberg, A. (1989). Structure and biology of cartilage and bone matrix noncollagenous macromolecules. *The FASEB Journal*, *3*(9), 2042–2051.
- Hoemann, C. D. (2004). Molecular and Biochemical Assays of Cartilage Components. In *Cartilage and Osteoarthritis* (pp. 127–156). Humana Press. https://doi.org/10.1385/1-59259-821-8:127
- Hölzl, K., Lin, S., Tytgat, L., Vlierberghe, S. Van, Gu, L., & Ovsianikov, A. (2016). Bioink properties before, during and after 3D bioprinting. *Biofabrication*, 8(3), 032002.
- Hunt, J. A., Chen, R., van Veen, T., & Bryan, N. (2014). Hydrogels for tissue engineering and regenerative medicine. *Journal of Materials Chemistry B*, 2(33), 5319–5338.
- Imhof, H., Breitenseher, M., Kainberger, F., Rand, T., & Trattnig, S. (1999). Importance of subchondral bone to articular cartilage in health and disease. *Topics in Magnetic Resonance Imaging*, *10*(3), 180–192. https://doi.org/10.1097/00002142-199906000-00002
- Khorshidi, S., & Karkhaneh, A. (2018). A review on gradient hydrogel/fiber scaffolds for osteochondral regeneration. *Journal of Tissue Engineering and Regenerative Medicine*, *12*(4), e1974–e1990. https://doi.org/10.1002/term.2628
- Kielty, C. M., Kwan, A. P. L., Holmes, D. F., Schor, S. L., & Grant, M. E. (1985). Type X collagen, a product of hypertrophic chondrocytes. *Biochemical Journal*, 227(2), 545–554. https://doi.org/10.1042/bj2270545
- Korah, L. V, Anilkumar, G., & Thomas, S. (2018). Hydrogels, DNA, and RNA polypeptides for the preparation of biomaterials. In *Fundamental Biomaterials: Polymers* (pp. 85–104). Woodhead Publishing. https://doi.org/10.1016/B978-0-08-

- 102194-1.00005-0
- Kulmala, K. A. M., Korhonen, R. K., Julkunen, P., Jurvelin, J. S., Quinn, T. M., Kröger, H., & Töyräs, J. (2010). Diffusion coefficients of articular cartilage for different CT and MRI contrast agents. *Medical Engineering and Physics*, *32*(8), 878–882. https://doi.org/10.1016/j.medengphy.2010.06.002
- Leddy, H. A., & Guilak, F. (2003). Site-specific molecular diffusion in articular cartilage measured using fluorescence recovery after photobleaching. *Annals of Biomedical Engineering*, *31*, 753–760. https://doi.org/10.1114/1.1581879
- Leddy, H. A., & Guilak, F. (2008). Site-specific effects of compression on macromolecular diffusion in articular cartilage. *Biophysical Journal*, *95*(10), 4890–4895. https://doi.org/10.1529/biophysj.108.137752
- Levingstone, T. J., Matsiko, A., Dickson, G. R., O'Brien, F. J., & Gleeson, J. P. (2014). A biomimetic multi-layered collagen-based scaffold for osteochondral repair. *Acta Biomaterialia*, *10*, 1996–2004. https://doi.org/10.1016/j.actbio.2014.01.005
- Li, B., & Aspden, R. M. (1997). Mechanical and material properties of the subchondral bone plate from the femoral head of patients with osteoarthritis or osteoporosis. *Annals of the Rheumatic Diseases*, 56(4), 247–254.
- Liu, A., Jennings, L. M., Ingham, E., & Fisher, J. (2015). Tribology studies of the natural knee using an animal model in a new whole joint natural knee simulator. *Journal of Biomechanics*, 48(12), 3004–3011. https://doi.org/10.1016/j.jbiomech.2015.07.043
- Loh, Q. L., & Choong, C. (2013). Three-dimensional scaffolds for tissue engineering applications: Role of porosity and pore size. *Tissue Engineering Part B: Reviews*, 19(6), 485–502. https://doi.org/10.1089/ten.teb.2012.0437
- Lories, R. J., & Luyten, F. P. (2011). The bone–cartilage unit in osteoarthritis. *Nature Reviews Rheumatology*, 7(1), 43–49. https://doi.org/10.1038/nrrheum.2010.197
- Lotke, P. A., & Granda, J. L. (1971). Changes in the penneability of human articular cartilage in early degenerative osteoarthritis. *Surgical Forum*, 22, 449–450.
- Lotke, P. A., & Granda, J. L. (1972). Alterations in the permeability of articular cartilage by proteolytic enzymes. *Arthritis & Rheumatism*, *15*(3), 302–308.
- Madry, H., van Dijk, C. N., & Mueller-Gerbl, M. (2010). The basic science of the subchondral bone. *Knee Surgery, Sports Traumatology, Arthroscopy*, *18*(4), 419–433. https://doi.org/10.1007/s00167-010-1054-z
- Mahjoub, M., Berenbaum, F., & Houard, X. (2012). Why subchondral bone in osteoarthritis? the importance of the cartilage bone interface in osteoarthritis. *Osteoporosis International*, 23(8), 841–846. https://doi.org/10.1007/s00198-012-2161-0
- Mansour, J. M. (2003). Biomechanics of cartilage. In *Kinesiology: the mechanics and pathomechanics of human movement* (pp. 66–79). Lippincott Williams and Wilkins.
- Mauck, R. L., Hung, C. T., & Ateshian, G. A. (2003). Modeling of Neutral Solute Transport in a Dynamically Loaded Porous Permeable Gel: Implications for Articular Cartilage Biosynthesis and Tissue Engineering. *Journal of Biomechanical Engineering*, 125(5), 602–614.
- Mente, P. L., & Lewis, J. L. (1994). Elastic modulus of calcified cartilage is an order of magnitude less than that of subchondral bone. *Journal of Orthopaedic Research*, 12(5), 637–647. https://doi.org/10.1002/jor.1100120506
- Miri, A. K., Hosseinabadi, H. G., Cecen, B., Hassan, S., & Zhang, Y. S. (2018). Permeability mapping of gelatin methacryloyl hydrogels. *Acta Biomaterialia*, 77, 38–47. https://doi.org/10.1016/j.actbio.2018.07.006
- Moses, M. A., Sudhalter, J., & Langer, R. (1990). Identification of an Inhibitor of Neovascularization from Cartilage. *Science*, 248(4961), 1408–1410.

- Mukherjee, S., Nazemi, M., Jonkers, I., & Geris, L. (2020). Use of Computational Modeling to Study Joint Degeneration: A Review. *Frontiers in Bioengineering and Biotechnology*, 8, 93. https://doi.org/10.3389/fbioe.2020.00093
- Naghieh, S., & Chen, X. (2021). Printability—A key issue in extrusion-based bioprinting. *Journal of Pharmaceutical Analysis*, 11(5), 564–579. https://doi.org/10.1016/j.jpha.2021.02.001
- Nair, N., Kim, W., Braatz, R. D., & Strano, M. S. (2008). Dynamics of Surfactant-Suspended Single-Walled Carbon Nanotubes in a Centrifugal Field. *Langmuir*, 24(5), 1790–1795.
- Nooeaid, P., Salih, V., Beier, J. P., & Boccaccini, A. R. (2012). Osteochondral tissue engineering: Scaffolds, stem cells and applications. *Journal of Cellular and Molecular Medicine*, *16*(10), 2247–2270. https://doi.org/10.1111/j.1582-4934.2012.01571.x
- Nowicki, M., Zhu, W., Sarkar, K., Rao, R., & Zhang, L. G. (2020). 3D printing multiphasic osteochondral tissue constructs with nano to micro features via PCL based bioink. *Bioprinting*, *17*, e00066. https://doi.org/10.1016/j.bprint.2019.e00066
- Oliviero, F., Ramonda, R., & Punzi, L. (2010). New horizons in osteoarthritis. *Swiss Med Wkly*, *37*. https://doi.org/10.4414/smw.2010.13098
- Pape, D., Filardo, G., Kon, E., van Dijk, C. N., & Madry, H. (2010). Disease-specific clinical problems associated with the subchondral bone. *Knee Surgery, Sports Traumatology, Arthroscopy*, *18*(4), 448–462. https://doi.org/10.1007/s00167-010-1052-1
- Pepelanova, I., Kruppa, K., Scheper, T., & Lavrentieva, A. (2018). Gelatin-Methacryloyl (GelMA) Hydrogels with Defined Degree of Functionalization as a Versatile Toolkit for 3D Cell Culture and Extrusion Bioprinting. *Bioengineering*, 5(3), 55. https://doi.org/10.3390/bioengineering5030055
- Peters, A. E., Akhtar, R., Comerford, E. J., & Bates, K. T. (2018). Tissue material properties and computational modelling of the human tibiofemoral joint: A critical review. *PeerJ*, 6, e4298. https://doi.org/10.7717/peerj.4298
- Poole, A. R., Matsui, Y., Hinek, A., & Lee, E. R. (1989). Cartilage macromolecules and the calcification of cartilage matrix. *The Anatomical Record*, 224(2), 167–179. https://doi.org/10.1002/ar.1092240207
- Pouran, B., Arbabi, V., Zadpoor, A. A., & Weinans, H. (2016). Isolated effects of external bath osmolality, solute concentration, and electrical charge on solute transport across articular cartilage. *Medical Engineering & Physics*, 38(12), 1399–1407.
- Rastogi, P., & Kandasubramanian, B. (2019). Review of alginate-based hydrogel bioprinting for application in tissue engineering. *Biofabrication*, 11(4). https://doi.org/10.1088/1758-5090/ab331e
- Redler, I., Mow, V. C., Zimny, M. L., & Mansell, J. (1975). The ultrastructure and biomechanical significance of the tidemark of articular cartilage. *Clinical Orthopaedics and Related Research*, *112*, 357–362. https://doi.org/10.1097/00003086-197510000-00038
- Schadow, S., Siebert, H. C., Lochnit, G., Kordelle, J., Rickert, M., & Steinmeyer, J. (2013). Collagen Metabolism of Human Osteoarthritic Articular Cartilage as Modulated by Bovine Collagen Hydrolysates. *PLoS ONE*, 8(1), e53955. https://doi.org/10.1371/journal.pone.0053955
- Schmidt, M. B., Mow, V. C., Chun, L. E., & Eyre, D. R. (1990). Effects of proteoglycan extraction on the tensile behavior of articular cartilage. *Journal of Orthopaedic Research*, 8(3), 353–363. https://doi.org/10.1002/jor.1100080307
- Setton, L. A., Mow, V. C., Miiller, F. J., Pita, J. C., & Howell, D. S. (1994). Mechanical Properties of Canine Articular Cartilage Are Significantly Altered Following

- Transection of the Anterior Cruciate Ligament. *Journal of Orthopaedic Research*, 12(4), 451–463.
- Sophia Fox, A. J., Bedi, A., & Rodeo, S. A. (2009). The Basic Science of Articular Cartilage: Structure, Composition, and Fuction. *Sports Health*, *1*(6), 461–468. https://doi.org/10.1177/1941738109350438
- Spicer, C. D. (2020). Hydrogel scaffolds for tissue engineering: The importance of polymer choice. *Polymer Chemistry*, *11*(2), 184–219. https://doi.org/10.1039/c9py01021a
- Tuan, R. S., Chen, A. F., & Klatt, B. A. (2013). Cartilage regeneration. *The Journal of the American Academy of Orthopaedic Surgeons*, 21(5), 303–311.
- Varma, M. V., Kandasubramanian, B., & Ibrahim, S. M. (2020). 3D printed scaffolds for biomedical applications. *Materials Chemistry and Physics*, 255, 123642. https://doi.org/10.1016/j.matchemphys.2020.123642
- Viceconti, M., Olsen, S., Nolte, L. P., & Burton, K. (2005). Extracting clinically relevant data from finite element simulations. *Clinical Biomechanics*, 20(5), 451–454. https://doi.org/10.1016/j.clinbiomech.2005.01.010
- Wang, L., Neumann, M., Fu, T., Li, W., Cheng, X., & Su, B. L. (2018). Porous and responsive hydrogels for cell therapy. *Current Opinion in Colloid and Interface Science*, *38*, 135–157. https://doi.org/10.1016/j.cocis.2018.10.010
- Westacott, C. (2002). Interactions between subchondral bone and cartilage in OA. Cells from osteoarthritic bone can alter cartilage metabolism. *Journal of Musculoskeletal Neuronal Interactions*, 2(6), 507–509.
- Woo, S. L. Y., Akeson, W. H., & Jemmott, G. F. (1976). Measurements of nonhomogeneous, directional mechanical properties of articular cartilage in tension. *Journal of Biomechanics*, 9(12), 785–791. https://doi.org/10.1016/0021-9290(76)90186-X
- Zhang, B., Huang, J., & Narayan, R. J. (2020). Gradient scaffolds for osteochondral tissue engineering and regeneration. *Journal of Materials Chemistry B*, 8(36), 8149–8170. https://doi.org/10.1039/d0tb00688b

# Appendix A

*Table 1.1:* Diffusion coefficients selected for all 12 layers of the computational model for each value of k and the values obtained from Arbabi et al. (2016).

#### Diffusion Coefficient (µm²/s)

|                            | Arbabi et al.<br>(2016) | k = 0.015 | k = 0.1 | k = 1/3 | k = 1  | k = 2  | k = 3 |
|----------------------------|-------------------------|-----------|---------|---------|--------|--------|-------|
| d <sub>Superficail_1</sub> | 4.35                    | 4.35      | 4.35    | 4.35    | 4.35   | 4.35   | 4.35  |
| d <sub>Superficial_2</sub> | 4.35                    | 0.2694    | 1.022   | 2.448   | 3.965  | 4.315  | 4.347 |
| d <sub>Middle_1</sub>      | 0.40                    | 0.2268    | 0.783   | 1.954   | 3.581  | 4.21   | 4.325 |
| d <sub>Middle_2</sub>      | 0.40                    | 0.2016    | 0.6354  | 1.607   | 3.196  | 4.035  | 4.264 |
| d <sub>Middle_3</sub>      | 0.40                    | 0.1837    | 0.527   | 1.331   | 2.812  | 3.791  | 4.147 |
| d <sub>Middle_4</sub>      | 0.40                    | 0.1697    | 0.4407  | 1.098   | 2.427  | 3.476  | 3.953 |
| d <sub>Middle_5</sub>      | 0.40                    | 0.1583    | 0.3688  | 0.8938  | 2.043  | 3.091  | 3.664 |
| d <sub>Deep_1</sub>        | 0.18                    | 0.1486    | 0.3069  | 0.7116  | 1.658  | 2.637  | 3.26  |
| d <sub>Deep_2</sub>        | 0.18                    | 0.1402    | 0.2526  | 0.546   | 1.274  | 2.113  | 2.723 |
| d <sub>Deep_3</sub>        | 0.18                    | 0.1327    | 0.204   | 0.3937  | 0.8891 | 1.518  | 2.033 |
| d <sub>Subchondral_1</sub> | 0.12                    | 0.126     | 0.1601  | 0.2523  | 0.5045 | 0.8541 | 1.172 |
| d <sub>Subchondral_2</sub> | 0.12                    | 0.12      | 0.12    | 0.12    | 0.12   | 0.12   | 0.12  |

*Table 1.2:* Values of the solid volume fraction for all 12 layers of the computational model for each value of k and the values obtained from Arbabi et al. (2016).

#### **Solid Volume Fraction**

|                            | Arbabi et al.<br>(2016) | k = 0.015 | k = 0.1 | k = 1/3 | k = 1  | k = 2  | k = 3  |
|----------------------------|-------------------------|-----------|---------|---------|--------|--------|--------|
| d <sub>Superficail_1</sub> | 0.20                    | 0.20      | 0.20    | 0.20    | 0.20   | 0.20   | 0.20   |
| d <sub>Superficial_2</sub> | 0.20                    | 0.7788    | 0.6721  | 0.4698  | 0.2545 | 0.205  | 0.2005 |
| d <sub>Middle_1</sub>      | 0.30                    | 0.7849    | 0.706   | 0.5399  | 0.3091 | 0.2198 | 0.2036 |
| d <sub>Middle_2</sub>      | 0.30                    | 0.7884    | 0.7269  | 0.5891  | 0.3636 | 0.2446 | 0.2122 |
| d <sub>Middle_3</sub>      | 0.30                    | 0.791     | 0.7423  | 0.6283  | 0.4182 | 0.2793 | 0.2289 |
| d <sub>Middle_4</sub>      | 0.30                    | 0.7929    | 0.7545  | 0.6613  | 0.4727 | 0.324  | 0.2563 |
| d <sub>Middle_5</sub>      | 0.30                    | 0.7946    | 0.7647  | 0.6902  | 0.5273 | 0.3785 | 0.2974 |
| d <sub>Deep_1</sub>        | 0.40                    | 0.7959    | 0.7735  | 0.7161  | 0.5818 | 0.443  | 0.3546 |
| d <sub>Deep_2</sub>        | 0.40                    | 0.7971    | 0.7812  | 0.7396  | 0.6364 | 0.5174 | 0.4308 |
| d <sub>Deep_3</sub>        | 0.40                    | 0.7982    | 0.7881  | 0.7612  | 0.6909 | 0.6017 | 0.5286 |
| d <sub>Subchondral_1</sub> | 0.80                    | 0.7991    | 0.7943  | 0.7812  | 0.7455 | 0.6959 | 0.6508 |
| d <sub>Subchondral_2</sub> | 0.80                    | 0.80      | 0.80    | 0.80    | 0.80   | 0.80   | 0.80   |

*Table 2.3:* Values of the elastic modulus for all 12 layers of the computational model for each value of k and the values obtained from Arbabi et al. (2016).

### E modulus (MPa)

|                            | Arbabi et<br>al. (2016) | k = 0.015 | k = 0.1 | k = 1/3 | k = 1 | k = 2  | k = 3 |
|----------------------------|-------------------------|-----------|---------|---------|-------|--------|-------|
| d <sub>Superficail_1</sub> | 10                      | 10        | 10      | 10      | 10    | 10     | 10    |
| d <sub>Superficial_2</sub> | 10                      | 1110      | 906.9   | 522.6   | 113.6 | 19.42  | 10.86 |
| d <sub>Middle_1</sub>      | 10                      | 1121      | 971.3   | 655.8   | 217.3 | 47.69  | 16.85 |
| d <sub>Middle_2</sub>      | 10                      | 1128      | 1011    | 749.3   | 320.9 | 94.79  | 33.13 |
| d <sub>Middle_3</sub>      | 10                      | 1133      | 1040    | 823.7   | 424.5 | 160.74 | 64.82 |
| d <sub>Middle_4</sub>      | 10                      | 1137      | 1064    | 886.5   | 528.2 | 245.54 | 117.1 |
| d <sub>Middle_5</sub>      | 10                      | 1140      | 1083    | 941.4   | 631.8 | 349.17 | 195.0 |
| d <sub>Deep_1</sub>        | 10                      | 1142      | 1100    | 990.6   | 735.5 | 471.65 | 303.8 |
| d <sub>Deep_2</sub>        | 10                      | 1145      | 1114    | 1035    | 839.1 | 612.98 | 448.5 |
| d <sub>Deep_3</sub>        | 10                      | 1147      | 1127    | 1076    | 942.7 | 773.14 | 634.4 |
| d <sub>Subchondral_1</sub> | 10                      | 1148      | 1139    | 1114    | 1046  | 952.15 | 866.5 |
| d <sub>Subchondral_2</sub> | 10                      | 1150      | 1150    | 1150    | 1150  | 1150   | 1150  |

## Appendix B

```
% This code returns FEBio file regarding different values of
% diffusivity
clc
clear all
close all
% Cartilage
d = 2.4;
x = [-d/2:d/11:d/2];
k = [0.015, 0.1, 1/3, 1, 2, 3];
Pb = 0.2;
Pt = 0.8;
vahid = [0.2, 0.2, 0.3, 0.3, 0.3, 0.3, 0.4, 0.4, 0.4, 0.8, 0.8];
vahid = flip(vahid,2);
SVF = powerplot(k,d,x,Pb,Pt,vahid);
save('SVF_BCU.mat','SVF')
n=1;
%Please define the intervals for SVF and FCD
load('SVF_BCU.mat');
for n=1:1:size(SVF,1)
% for n=3
for i=SVF(n,1)
for i2=SVF(n,2)
for j=SVF(n,3)
for j2=SVF(n,4)
for j3=SVF(n,5)
for j4=SVF(n,6)
for j5=SVF(n,7)
for k=SVF(n,8)
for k2=SVF(n,9)
for k3=SVF(n,10)
for g=SVF(n,11)
for g2=SVF(n,12)
    i2
    j
    j2
    j3
    j4
    j5
    k
    k2
    k3
    g
    g2
    % n=n+1;
```

```
fin = fopen('Refinement4.feb','r');
    % txt_name=['Jordi_File_3' '.feb'];
    txt_name=['Jordi_File_' num2str(n) '.feb'];
fout = fopen(txt_name,'w');
    idk=0;
    while ~feof(fin)
        idk=idk+1;
        s = fgetl(fin);
        %idk is the line number in FCD.feb file
        %We change the diffusivity of all layers to the i value
           if idk==69
               s=[blanks(20) '<phi0>' num2str(0.8) '</phi0>']; % any number
you want or within the loop s=['<diff>' num2str(i) '</diff>']; i is 1:100
        if idk==69
            s=[blanks(20) '<phi0>' num2str(i) '</phi0>']; % any number you
want or within the loop s=['<diff>' num2str(i) '</diff>']; i is 1:100
        end
        if idk==92
            s=[blanks(20) '<phi0>' num2str(i2) '</phi0>']; % any number you
want or within the loop s=[i<diff>2 num2str(i) '</diff>']; i is 1:100
        end
        if idk==115
            s=[blanks(20) '<phi0>' num2str(j) '</phi0>']; % any number you
want or within the loop s=[j<diff>' num2str(i) '</diff>']; i is 1:100
        if idk==138
            s=[blanks(20) '<phi0>' num2str(j2) '</phi0>']; % any number you
want or within the loop s=[j<diff>2 num2str(i) '</diff>']; i is 1:100
        if idk==161
            s=[blanks(20) '<phi0>' num2str(j3) '</phi0>']; % any number you
want or within the loop s=[j<diff>2 num2str(i) '</diff>']; i is 1:100
        if idk==184
            s=[blanks(20) '<phi0>' num2str(j4) '</phi0>']; % any number you
want or within the loop s=[j< diff>2 \quad num2str(i) \quad 4</diff>']; i is 1:100
        if idk==207
            s=[blanks(20) '<phi0>' num2str(j5) '</phi0>']; % any number you
want or within the loop s=[j<diff>2 num2str(i) 5</diff>']; i is 1:100
        end
        if idk==230
            s=[blanks(20) '< phi0>' num2str(k) '</phi0>']; % any number you
want or within the loop s=[j<diff>2 num2str(i) k</diff>']; i is 1:100
        end
        if idk==253
            s=[blanks(20) '<phi0>' num2str(k2) '</phi0>']; % any number you
want or within the loop s=[j< diff>2 \quad num2str(i) \quad k</diff>']; i is 1:100
        end
        if idk==276
            s=[blanks(20) '<phi0>' num2str(k3) '</phi0>']; % any number you
want or within the loop s=[j<diff>2 num2str(i) k</diff>']; i is 1:100
        end
        if idk==299
            s=[blanks(20) '<phi0>' num2str(g) '</phi0>']; % any number you
want or within the loop s=[j<diff>2 num2str(i) g</diff>']; i is 1:100
        end
        if idk==322
```

```
s=[blanks(20) '<phi0>' num2str(g2) '</phi0>']; % any number you
want or within the loop s=[j<diff>2 num2str(i) g</diff>']; i is 1:100
                     fprintf(fout, '%s\n',s);
          end
          fclose(fin);
          fclose(fout);
end
%Run the file
% system ('Jordi File 3.feb');
for kk=1:size(SVF,1)
% for kk=1
          filename = sprintf('Jordi_File_%d.feb', kk);
          system([filename, '&'])
end
\(\sigma\)\(\sigma\)\(\sigma\)\(\sigma\)\(\sigma\)\(\sigma\)\(\sigma\)\(\sigma\)\(\sigma\)\(\sigma\)\(\sigma\)\(\sigma\)\(\sigma\)\(\sigma\)\(\sigma\)\(\sigma\)\(\sigma\)\(\sigma\)\(\sigma\)\(\sigma\)\(\sigma\)\(\sigma\)\(\sigma\)\(\sigma\)\(\sigma\)\(\sigma\)\(\sigma\)\(\sigma\)\(\sigma\)\(\sigma\)\(\sigma\)\(\sigma\)\(\sigma\)\(\sigma\)\(\sigma\)\(\sigma\)\(\sigma\)\(\sigma\)\(\sigma\)\(\sigma\)\(\sigma\)\(\sigma\)\(\sigma\)\(\sigma\)\(\sigma\)\(\sigma\)\(\sigma\)\(\sigma\)\(\sigma\)\(\sigma\)\(\sigma\)\(\sigma\)\(\sigma\)\(\sigma\)\(\sigma\)\(\sigma\)\(\sigma\)\(\sigma\)\(\sigma\)\(\sigma\)\(\sigma\)\(\sigma\)\(\sigma\)\(\sigma\)\(\sigma\)\(\sigma\)\(\sigma\)\(\sigma\)\(\sigma\)\(\sigma\)\(\sigma\)\(\sigma\)\(\sigma\)\(\sigma\)\(\sigma\)\(\sigma\)\(\sigma\)\(\sigma\)\(\sigma\)\(\sigma\)\(\sigma\)\(\sigma\)\(\sigma\)\(\sigma\)\(\sigma\)\(\sigma\)\(\sigma\)\(\sigma\)\(\sigma\)\(\sigma\)\(\sigma\)\(\sigma\)\(\sigma\)\(\sigma\)\(\sigma\)\(\sigma\)\(\sigma\)\(\sigma\)\(\sigma\)\(\sigma\)\(\sigma\)\(\sigma\)\(\sigma\)\(\sigma\)\(\sigma\)\(\sigma\)\(\sigma\)\(\sigma\)\(\sigma\)\(\sigma\)\(\sigma\)\(\sigma\)\(\sigma\)\(\sigma\)\(\sigma\)\(\sigma\)\(\sigma\)\(\sigma\)\(\sigma\)\(\sigma\)\(\sigma\)\(\sigma\)\(\sigma\)\(\sigma\)\(\sigma\)\(\sigma\)\(\sigma\)\(\sigma\)\(\sigma\)\(\sigma\)\(\sigma\)\(\sigma\)\(\sigma\)\(\sigma\)\(\sigma\)\(\sigma\)\(\sigma\)\(\sigma\)\(\sigma\)\(\sigma\)\(\sigma\)\(\sigma\)\(\sigma\)\(\sigma\)\(\sigma\)\(\sigma\)\(\sigma\)\(\sigma\)\(\sigma\)\(\sigma\)\(\sigma\)\(\sigma\)\(\sigma\)\(\sigma\)\(\sigma\)\(\sigma\)\(\sigma\)\(\sigma\)\(\sigma\)\(\sigma\)\(\sigma\)\(\sigma\)\(\sigma\)\(\sigma\)\(\sigma\)\(\sigma\)\(\sigma\)\(\sigma\)\(\sigma\)\(\sigma\)\(\sigma\)\(\sigma\)\(\sigma\)\(\sigma\)\(\sigma\)\(\sigma\)\(\sigma\)\(\sigma\)\(\sigma\)\(\sigma\)\(\sigma\)\(\sigma\)\(\sigma\)\(\sigma\)\(\sigma\)\(\sigma\)\(\sigma\)\(\sigma\)\(\sigma\)\(\sigma\)\(\sigma\)\(\sigma\)\(\sigma\)\(\sigma\)\(\sigma\)\(\sigma\)\(\sigma\)\(\sigma\)\(\sigma\)\(\sigma\)\(\sigma\)\(\sigma\)\(\sigma\)\(\sigma\)\(\sig
disp('Press a key when system is ready to continue')
pause;
%%
clear all;
clc;
load('SVF_BCU.mat');
for kk=1:1:size(SVF,1)
% kk=3;
%% Add functions path to matlab search path
functionname='ReadData.m';
functiondir=which(functionname);
% functiondir=functiondir(1:end-length(functionname));
% addpath(genpath([functiondir 'D0 W0 L0 G5 T0 F1 P37 X0 Y0']));
% addpath(genpath([functiondir 'Healthy Model_Experiment']));
%%%%%
%%
%num add=84:
[filename_txt,pathname_txt] = sprintf('Jordi_file_%d.log',kk);
txtfile=[pathname_txt filename_txt];
s=cell(1200000,1);
sizS=1200000;
```

```
lineCt=1;
% Calculate
fid=fopen(txtfile);
tline=fgetl(fid);
while ischar(tline)
    s{lineCt}=tline;
    lineCt=lineCt+1;
    % grow s if necessary
    if lineCt>sizS
        s=[s; cell(1200000,1)];
        sizS=sizS+1200000;
    end
    tline=fgetl(fid);
end
%remove empty entries in s:
s(lineCt:end)=[];
% Index DataRecord step3=strfind(s,'converged at time : 1101');
Index DataRecord Final Row step3=find(not(cellfun('isempty',Index DataRecord ste
p3)));
% Row to Read DataRecord step3=Index DataRecord Final Row step3+2;
% A=size(s);
% Index Increment Final step3=Row to Read DataRecord step3+1+A(1,1)-
Row to Read DataRecord step3;
% for dd=1:Row_to_Read_DataRecord_step3
% s{dd}='vahid';
% end
ss=s;
Index_DataRecord_time=strfind(ss,'converged at time :');
Index_DataRecord_Final_Row_time=find(not(cellfun('isempty',Index_DataRecord_time)
)));
A=size(Index DataRecord Final Row time);
t(1)=0;
for bb=1:A(1,1)
    ss time(bb)=ss(Index DataRecord Final Row time(bb));
    t(bb+1)= sscanf(ss_time{bb}, '----- converged at time :%f');
end
ss time=ss time';
% t=t-1101;
% t=t';
Index_DataRecord=strfind(s,'Data Record');
Index DataRecord Final Row=find(not(cellfun('isempty',Index DataRecord)));
Row to Read DataRecord=Index DataRecord Final Row+5;
Index Increment Final=Index DataRecord Final Row+4+151;
Mx=zeros(151,length(Index Increment Final));
M=zeros(151,length(Index Increment Final));
for i=1:length(Index_Increment_Final)
       Mx(:,i)=textread([pathname_txt filename_txt],'%*f %f', 151,'headerlines',
Row to Read DataRecord(i)-1);
```

```
M(1:16,i)=Mx(136:151,i);
                    M(17:40,i)=Mx(112:135,i);
                   M(41:80,i)=Mx(72:111,i);
                    M(81:96,i)=Mx(56:71,i);
                   M(97:151,i)=Mx(1:55,i);
end
txt_name=['FCDout_' num2str(kk) '.txt'];
save (txt name, 'M', '-ASCII')
txt_name_time=['t_' num2str(kk) '.txt'];
save (txt name time, 't', '-ASCII')
clear all
end
\(\sigma\sigma\sigma\sigma\sigma\sigma\sigma\sigma\sigma\sigma\sigma\sigma\sigma\sigma\sigma\sigma\sigma\sigma\sigma\sigma\sigma\sigma\sigma\sigma\sigma\sigma\sigma\sigma\sigma\sigma\sigma\sigma\sigma\sigma\sigma\sigma\sigma\sigma\sigma\sigma\sigma\sigma\sigma\sigma\sigma\sigma\sigma\sigma\sigma\sigma\sigma\sigma\sigma\sigma\sigma\sigma\sigma\sigma\sigma\sigma\sigma\sigma\sigma\sigma\sigma\sigma\sigma\sigma\sigma\sigma\sigma\sigma\sigma\sigma\sigma\sigma\sigma\sigma\sigma\sigma\sigma\sigma\sigma\sigma\sigma\sigma\sigma\sigma\sigma\sigma\sigma\sigma\sigma\sigma\sigma\sigma\sigma\sigma\sigma\sigma\sigma\sigma\sigma\sigma\sigma\sigma\sigma\sigma\sigma\sigma\sigma\sigma\sigma\sigma\sigma\sigma\sigma\sigma\sigma\sigma\sigma\sigma\sigma\sigma\sigma\sigma\sigma\sigma\sigma\sigma\sigma\sigma\sigma\sigma\sigma\sigma\sigma\sigma\sigma\sigma\sigma\sigma\sigma\sigma\sigma\sigma\sigma\sigma\sigma\sigma\sigma\sigma\sigma\sigma\sigma\sigma\sigma\sigma\sigma\sigma\sigma\sigma\sigma\sigma\sigma\sigma\sigma\sigma\sigma\sigma\sigma\sigma\sigma\sigma\sigma\sigma\sigma\sigma\sigma\sigma\sigma\sigma\sigma\sigma\sigma\sigma\sigma\sigma\sigma\sigma\sigma\sigma\sigma\sigma\sigma\sigma\sigma\sigma\sigma\sigma\sigma\sigma\sigma\sigma\sigma\sigma\sigma\sigma\sigma\sigma\sigma\sigma\sigma\sigma\sigma\sigma\sigma\sigma\sigma\sigma\sigma\sigma\sigma\sigma\sigma\sigma\sigma\sigma\sigma\sigma\sigma\sigma\sigma\sigma\sigma\sigma\sigma\sigma\sigma\sigma\sigma\sigma\sigma\sigma\sigma\sigma\sigma\sigma\sigma\sigma\sigma\sigma\sigma\sigma\sigma\sigma\sigma\sigma\sigma\sigma\sigma\sigma\sigma\sigma\sigma\sigma\sigma\sigma\sigma\sigma\sigma\sigma\sigma\sigma\sigma\sigma\sigma\sigma\sigma\sigma\sigma\sigma\sigma\sigma\sigma\sigma\sigma\sigma\sigma\sigma\sigma\sigma\sigma\sigma\sigma\sigma\sigma\sigma\sigma\sigma\sigma\sigma\sigma\sigma\sigma\sigma\sigma\sigma\sigma\sigma\sigma\sigma\sigma\sigma\sigma\sigma\sigma\sigma\sigma\sigma\sigma\sigma\sigma\sigma\sigma\sigma\sigma\sigma\sigma\sigma\sigma\sigma\sigma\sigma\sigma\sigma\sigma\sigma\sigma\sigma\sig
%%
clc
clear all
format long
close all
load('SVF BCU.mat');
%In this code first we will resume concentration and time data from FCDout
%files, then we remove the data related to bath.
ss=size(SVF,1);
% ss=1;
for j=1:1:ss
% for j=ss:1:ss
           j
k=num2str(j);
txt_name=['FCDout_' num2str(j) '.txt'];
ce=load (txt_name);
   ce(97:151,:)=[];
ce(1:16,:)=[];
txt_name_time=['t_' num2str(j) '.txt'];
t=load (txt name time);
t(1)=[];
t=t';
n=size(t);
% ce=ce(1:n(1,1),51:165);
load thick cartilage.txt;
ce feb=ce'*thick cartilage';
ce_feb=ce_feb/(0.9*420);
figure(1)
% subplot(2,1,1);
plot(t/3600,100*ce_feb, '--', 'LineWidth', 1);
xlabel('Time [h]');
ylabel('Nomalized Concentration (% bath)');
load t exp.txt
load c_exp_norm.txt
% t_exp(1)=[];
% c_exp_norm(1)=[];
% m=size(t_exp)
% for i=1:m(1,1)
```

```
% c_feb_interp(i)=interp1(t,ce_feb,3600*t_exp(i));
% end;
hold on
%plot(t_exp,100*c_feb_interp,'o');
% rmse tutorial.
% One way is to use the Root Mean Square function and pass in the "error" part.
% rmse = rms(Predicted-Actual)
% That's it! You're done.
% But for those of you who are the curious type,
% here's how to calculate the root-mean-square-error by hand.
% First calculate the "error".
% err = c_exp_norm/100 - c_feb_interp';
% Then "square" the "error".
% squareError = err.^2;
% Then take the "mean" of the "square-error".
% meanSquareError = mean(squareError);
% Then take the "root" of the "mean-square-error" to get
% the root-mean-square-error!
% rootMeanSquareError(j) = sqrt(meanSquareError)
% rmse = rms(c_exp_norm/100 - c_feb_interp')
% % So, this is true.
% % rootMeanSquareError == rmse
end
figure(1)
% subplot(2,1,1);
% plot(t_exp,c_exp_norm,'diamond', 'MarkerFaceColor',[0.3010 0.7450 0.9330])
% legend('k = 0.015', 'k = 0.1', 'k = 1/3', 'k = 1', 'k = 2', 'k = 3',
'Refined', 'Experimental data')
legend('k = 0.015', 'k = 0.1', 'k = 1/3', 'k = 1', 'k = 1', 'k = 1', 'Refined')
%%
clc
clear all
format long
close all
load('SVF_BCU.mat');
%In this code first we will resume concentration and time data from FCDout_
%files, then we remove the data related to bath.
% ss=size(SVF,1);
ss=size(SVF,1)-1;
% ss=1
for j=1:1:ss
% for j=ss:1:ss
k=num2str(j);
txt_name=['FCDout_' num2str(j) '.txt'];
```

```
ce=load (txt name);
ce=ce(1:16,:);
txt_name_time=['t_' num2str(j) '.txt'];
t=load (txt_name_time);
t(1)=[];
t=t;
n=size(t);
% ce=ce(1:n(1,1),51:165);
load thick subchondral.txt;
ce feb=ce'*thick_subchondral';
ce feb=ce feb/(0.1782*420);
figure(2)
% subplot(2,1,2);
data1=plot(t/3600,100*ce_feb, 'LineWidth', 1);
hold on
%legend('2');
xlabel('Time [h]');
ylabel('Nomalized Concentration (%bath)');
t2=t/3600;
dt=mean(diff(t2));
y=100*ce feb;
dy=gradient(y,dt);
dy2=dy(500:end);
idx=find(dy2 <= 0.001)+500;
idt(j)=idx(1);
t eq(j)=t2(idt(j));
ce_eq(j)=y(idt(j));
figure(2)
fit=plot(t_eq(j), ce_eq(j), 'p', 'LineWidth', 2);
fit.SeriesIndex = data1.SeriesIndex;
hold on
end
figure(2)
% subplot(2,1,2);
% plot(t_exp,c_exp_norm_sub,'diamond', 'MarkerFaceColor',[0.3010 0.7450 0.9330])
% legend('k = 0.015', 'k = 0.1', 'k = 1/3', 'k = 1', 'k = 2', 'k = 3',
'Refined', 'Experimental data')
% plot(t_eq, ce_eq, 'p', 'Color', 'b', 'LineWidth', 2);
plot(nan,nan, 'p', 'Color', 'k', 'LineWidth', 2);
legend('k = 0.015', '', 'k = 0.1', '', 'k = 1/3', '', 'k = 1', '', 'k = 2', '',
'k = 3', '', 'Near-Equilibrium Time')
k=[0.015, 0.1, 1/3, 1, 2, 3];
figure(3)
plot(k, t_eq(1:6), '--o', 'MarkerFaceColor', [0 0.4470 0.7410])
xlabel('k')
ylabel('Near-equilibrium time [h]')
xlim([-1,4]);
ylim([0,2500]);
```